Revision 2

3/07/2023

Word count = 5158

Crystal Growth According to the Law of Proportionate Effect

D.D. Eberl

349 Mountain Meadows Road, Boulder, Colorado 80302, U.S.A

ddeberl@gmail.com

ABSTRACT

This paper summarizes an approach to crystal growth that was published in parts in a variety of articles over the course of 25 years by the present author and his colleagues. Evidence for this approach, which is confirmed in detail by data in the cited publications and in the figures and equations in the supplementary material that accompanies this paper, comes mainly from the shapes of crystal size distributions (CSDs). Such distributions reveal the growth histories of natural minerals and synthetic compounds, histories that can be used to make geological interpretations and to guide industrial syntheses.

CSDs have three fundamental shapes: lognormal, asymptotic and Ostwald. These shapes result from different degrees of supersaturation near the time of nucleation. The first two distribution shapes form according to the Law of Proportionate Effect (LPE) at moderate supersaturation, and the latter rare distribution forms by Ostwald ripening at large supersaturation. Initially, the first two distributions have mean diameters of up to tens of nanometers and grow by surface-limited growth kinetics. The slow step in this reaction is the incorporation of nanoparticles (bits of crystal or adparticles) onto the crystal surface. As

the crystals become larger their demand for nutrients, as calculated by the LPE, increases exponentially. Then the slow step in the reaction changes to the rate of transfer of nutrients to the crystal (supply- or transport-limited growth). Crystal diameters often grow the most during this latter stage, and the initial CSD shapes that originally formed during surface-limited growth are retained and scaled up proportionately.

Proportionate growth during the supply-limited stage can be simulated approximately by multiplying the diameter of each crystal in a distribution by a constant. Crystals also can grow by a constant rate law in which a constant length is added to each crystal diameter in the distribution. This rare process causes the original CSD to narrow so that its initial shape is not preserved. The growth law that prevails, either proportionate or constant, is determined by the manner in which nutrients are supplied to the crystal. Supply is by advective flow during proportionate growth, with the nutrient solution moving with respect to the crystals. Constant growth relies on the random diffusion of nutrients through a quiescent solution. Proportionate growth is by far the most common growth law, and therefore nutrient supply by diffusion alone during crystal growth is uncommon.

Distributions formed by Oswald ripening, and those formed by other rare processes, also are discussed. During Ostwald ripening, nucleation caused by mixing reactants at large supersaturation forms crystals that are extremely fine and numerous. The larger crystals grow at the expense of the finer, less stable crystals, thereby forming, on completion, the universal steady-state CSD shape predicted by the Lifshitz-Slyozov-Wagner (LSW) theory. This unique CSD shape, as well as other rare shapes, then are scaled up to larger sizes by supply-limited proportionate growth.

This is the peer-reviewed, final accepted version for American Mineralogist, published by the Mineralogical Society of America.
The published version is subject to change. Cite as Authors (Year) Title. American Mineralogist, in press.
DOI: https://doi.org/10.2138/am-2022-8851. http://www.minsocam.org/

Key words: Crystal growth, proportionate growth, constant growth, Ostwald ripening, crystal size distributions, Law of Proportionate Effect, crystallization, nucleation, stochastic crystal growth

GROWTH OF LOGNORMAL CRYSTAL SIZE DISTRIBUTIONS

Minerals most commonly have lognormal crystal size distributions (CSDs; Figs. 1, 15 and 17 in Eberl et al. 1998; Fig. 2 in Kile and Eberl 1999; Figs. 3 and 9 in Kile et al. 2000; Fig. 5b in Bove et al. 2002; Figs. 1 and 3 in Eberl et al. 2002a; Fig 3 in Kile and Eberl 2003; Figs. 5 and 7 in Badino et al. 2009; Fig. 3 in Eberl 2022). A lognormal distribution (Fig. 1) is described by the equation:

$$g(X) = \left[\frac{1}{X\beta\sqrt{2\pi}}\right] exp\left\{-\left(\frac{1}{2\beta^2}\right)[ln(X) - \alpha]^2\right\}, \qquad (1)$$

where *g(X)* is the continuous theoretical frequency distribution of variable *X*, where, in this case, the *X*s are crystal diameters that are parallel to a given crystallographic direction. Equation 1 can be solved if two parameters are known: α and β^2 are the mean and variance of the distribution of the natural logs of X. The original scale units for α need to be specified because it is a log. β^2 indicates the breadth of a distribution for a given α.

Iteration of the Law of Proportionate Effect (LPE) is the simple mathematical procedure that generates the lognormal distribution (Koch 1966) and thereby simulates crystal growth (Eberl et al. 2000):

$$X_{j+1} = X_j + \varepsilon_j X_j\,, \qquad (2)$$

where X_j is the diameter of an individual crystal, ε_j is a random number that varies independently for each crystal between 0 and 1, and *j* denotes the calculation cycle for the LPE iteration. Starting, for example, with 1000 crystals having a diameter of 1 nm, Equation 2 is solved *j* times

for each crystal by substituting X_{j+1} back into the equation for $X_{j,.}$ The distribution evolves from an even distribution into a lognormal one when the crystal sizes resulting from the LPE calculation are grouped into equally spaced bin sizes, using the bin centers as X. For example, sizes calculated by the LPE that range between 2.5 and 3.5 nm are grouped as 3 nm, and the number of crystals in the bin is noted. Continued iteration of the LPE leads to an increase in the mean size and variance of the distribution (Fig. 2 in Eberl et al. 1998).

The results of the LPE calculation are verified as being lognormal by calculating the parameters α and β^2 from the numbers of crystals in the binned LPE sizes, where $\alpha = \sum ln(X) f(X)$, and $\beta^2 = \sum [ln(X) - \alpha]^2 f(X)$, where $f(X)$ is the frequencies of binned crystal sizes X. The two parameters are entered into Equation 1, and the theoretical lognormal number of crystals for each binned size is calculated from Equation 1 by multiplying a normalized $g(X)$ times the total number of crystals counted, in this case 1000. This distribution is compared statistically (using the Chi-square test, or the Kolmogorov-Smirnov test for sparse data) to the distribution of crystals calculated from the LPE to verify the lognormal shape. The same general procedure is used to test measured distributions for log-normality.

The LPE is assumed to be the central equation that describes relative crystal growth rates in natural and synthetic systems because it duplicates the experimentally measured lognormal shapes of natural and synthetic CSDs (Eberl et al. 1998; Eberl et al. 2002a). The LPE models crystal growth as a stochastic process, as opposed to being deterministic. This means that although crystal growth has a random component (ε), this randomness follows a rule (the LPE). Therefore, although the relative growth rates of individual crystals can not be calculated precisely, the distribution shape calculated by iterating Equation 2 is predictably lognormal.

If the LPE is taken literally, it offers other insights into the growth process. The growth particles (termed nanoparticles, adparticles or colloids) that attach themselves to a crystal's surface are a random fraction of a crystal's initial size ($\varepsilon_j X_j$) rather than being individual atoms, ions or monomers. Such crystallization by oriented particle attachment is supported by electron micrographs that show diverse types of nanoparticles in various stages of attachment (e.g., Fig. 12 in Ivanov et. al. 2014; Fig. 2 in De Yoreo et. al. 2015). Atom by atom or molecule by molecule growth would not produce lognormal CSDs. Also, according to the LPE, growth by the coalescence of nanoparticles occurs in discrete cycles (j) rather than continuously.

The LPE also indicates that the relative rate of crystal growth is a function of the linear dimensions of the crystal (i.e., of its diameter X), rather than of its surface area or volume. In the older literature this type of growth was termed size dependent growth; but, more specifically, it is now termed proportionate growth. Whereas previously such growth was considered to be a rarity, proportionate growth is in fact the most common growth mechanism (Eberl et al. 1998). The random variable in the LPE also clarifies crystal growth dispersion, whereby individual crystals, all initially of the same size, and each subjected to identical growth environments, can grow at different rates (see Eberl et al. 1998, p. 503, for pertinent references).

The LPE (Equation 2) is not the complete story, because the predicted growth rate can not be sustained. Unconstrained iteration of the LPE leads to exponential growth, and eventually to very large adparticles and distribution variances (Figs. 2 and 3 in Eberl et al. 1998). However, Equation 2 applies only to the initial stages of growth, immediately during and after nucleation, when calculation of the growth rate is limited only by the incorporation of nanoparticles ($\varepsilon_j X_j$) onto the crystal surface. It is a rate that prevails at distribution mean sizes that range up to tens of nanometers (as indicated by Fig. 2 in Eberl et al. 1998). At larger sizes calculation of the

112 growth rate is limited by the rate of supply of material to the crystal, rather than by incorporation
113 onto the surface. Equation 2 is modified for supply-limited growth to account for a limited
114 volume of nutrients carried to the surfaces during each calculation cycle (j) of the LPE (for
115 details concerning this volume-limiting calculation see Equation 8 in Eberl et al. 1998, or
116 Equation 2 in Kile et al. 2000). This modification of the LPE leads to the calculation of
117 adparticles that are limited in size, that are small compared to the size of the growing crystal, and
118 that preserve β^2 during growth. Thus surface-limited growth initially gives the distribution a
119 lognormal shape, whereas subsequent supply-limited growth preserves this shape (meaning that
120 β^2 remains constant) as the mean size (α) increases (see Fig. 6 in Eberl et. al. 1998; Fig. 7 and
121 Table 2 for continuous growth experiments in Kile et al. 2000; see Fig. 3 for a similar
122 experiment in Eberl et al. 2002a).
123 The growth of a distribution during supply-limited growth can be duplicated approximately by
124 multiplying the crystal sizes in the distribution by a constant (k, which is a constant of
125 proportionality or scale factor). Equation 2 then reduces to $X_{(j+1)} = kX_j$, where the constant k
126 substitutes for the random variable $(1 + \varepsilon_j)$. This procedure increases the distribution's mean size
127 while keeping its variance constant. However, this calculation, although convenient, is not
128 completely satisfactory because multiplication by k does not express the random tendency for
129 growth found at small diameters. Multiplication by k causes the growth rate of individual
130 crystals to be predictable. A more realistic calculation applies the volume adjusted growth limit
131 for each iteration of the LPE, as was discussed above. The shape of the resulting distribution is
132 the same for either calculation, but the sizes of individual crystals differ because the latter
133 calculation contains a random number rather than a constant (Fig. 2B in Eberl et al. 2002a).

CSDs that have very different mean sizes, ranging from nanometers (e.g., illite crystal thicknesses; see Fig. 5b in Bove et al. 2002) to meters (giant gypsum crystals in Naica's Cueva de los Cristales that range to >11 m long; see Figs. 5 and 7 in Badino 2009), have lognormal shapes with similar variances (e.g., Fig. 16 in Eberl et al. 1998 and Fig. 7 in Kile et al. 2000). Such shapes most likely result from the proportionate growth of lognormal distributions that were formed according to LPE growth early in crystallization. Other growth mechanisms, such as ripening, constant growth or entirely random growth, would quickly destroy the lognormal shape and alter the variances (Fig. 8 in Eberl et al. 1998; Figs. 2 and 3 in Eberl et al. 2002a). Therefore, control of the initial CSD shape during and immediately after nucleation is key to controlling the shape of the final CSD because the earlier shape is scaled up during supply-limited growth.

FORMATION OF CSD SHAPES OTHER THAN LOGNORMAL

Diverse conditions near the time of nucleation can lead to a variety of CSD shapes. These shapes include the commonly found asymptotic CSD, and the rare Ostwald, transitional, non-Ostwald and multimodal CSDs.

Nucleation occurs in supersaturated solutions when crystals appear that have radii (r) greater than that of the critical radius (r*). If $r > r^*$ crystals can nucleate and grow. If $r < r^*$ they dissolve. A crystal having a size equal to r* is in equilibrium with the solution, and neither grows nor dissolves. A solution needs to be supersaturated, rather than simply saturated, to form growing nuclei because the saturation state for a mineral (i.e., its solubility product) is determined for the infinitely large crystal, and, therefore, does not address an increase in solubility related to an increase in specific surface energy for finer crystals. Furthermore, concentrations measured for a bulk solution do not address inhomogeneities present in a solution at the nanometer scale

(particularly upon mixing), further complicating the calculation of r*. In addition, the value for r* may increase during nucleation and growth if the saturation level falls as crystallization proceeds.

Experiments with calcite nucleation and growth and with computer simulation (Eberl et al. 1998; Kile et al. 2000; Eberl et al. 2000) indicate that variations in nucleation history can lead to CSD shapes that are not lognormal. For example, if nucleation occurs over an extended time at a constant or accelerating nucleation rate while previously formed nuclei grow according to the LPE, an asymptotic distribution (Fig. 1) results in which the smallest size category has the largest frequency (see also: Table 2 and Figs. 4 and 13 in Eberl et al. 1998; Fig. 2 in Kile et al. 2000). After an initial period of nucleation and growth, this shape can be preserved (β^2 is held constant) and scaled up by subsequent supply-limited proportionate growth, as was discussed. This commonly occurring asymptotic shape can be described approximately using the lognormal equation (Equation 1), but it doesn't often pass the statistical test. It can readily evolve into a lognormal shape if nucleation ceases while surface-limited growth continues (Figs. 6 and 7 in Bove et al. 2002).

A second complication in CSD shape is related to nucleation that occurs when concentrated solutions are suddenly mixed. Such an event, which is rare in nature, can lead to the universal steady state shape that is expected for supply-limited Ostwald ripening, a distribution that is skewed opposite to that of lognormal (Fig. 1). The equation for this shape was derived independently by Lifshitz and Slyozov (1961) and by Wagner (1961) in what is known as the LSW theory. As was similarly discussed for the lognormal distribution, the LSW equation that describes the Ostwald distribution (Equation A20 in Eberl et al. 1998) differs from the simple equation that is iterated to simulate the distribution (Equation 10 in Eberl et al. 1998, presented

by Markworth 1970). Experiments and calculations (Kile et al. 2000) have shown that this unique universal steady-state shape forms initially at very large levels of supersaturation, where abundant and extremely fine nuclei precipitate. A large contrast in specific surface areas among these particles leads to growth of the larger nuclei ($r>r^*$) at the expense of the dissolution or the incorporation of the smaller, less stable nuclei ($r<r^*$) according to the Ostwald ripening mechanism, with r^* approximated by the mean radius.

According to LSW theory, the CSD for any mineral that has undergone sufficient ripening will have the identical negatively skewed distribution shape when the data are plotted on reduced axes (size/mean size vs. frequency/maximum frequency), a shape that is independent from the initial, pre-ripened CSD shape, and that has a cutoff at large sizes (Fig. 1; see also Fig. 4 in Kile et al. 2000). The coincidence of CSDs on a reduced plot means that the variances are equal. The Ostwald shape, which has a constant and small variance of about 0.06, is scaled up by supply-limited growth, which leads to an increase in mean size while the variance is preserved. The resulting crystals all have nearly the same size (Fig. 8 in Kile et al. 2000).

The Ostwald CSD forms initially at large supersaturation, whereas the lognormal shape forms initially at smaller supersaturation. Nuclei precipitated at smaller saturation are larger and fewer, and therefore are less subject to ripening. Calcite crystallization experiments (Table 1 and Fig. 6 in Kile et al. 2000) showed that lognormal CSDs formed at initial omegas ranging from 22 to 40, where omega is defined as the ion activity product of the solution divided by the mineral solubility product. Therefore a solution with an omega of one is at equilibrium with a crystal that has negligible specific surface energy. However, the Ostwald CSD appeared at initial omegas >100, where nuclei formed having very large specific surface energies. Between these values (28 to 69) CSDs crystallized that had transitional shapes between lognormal and Ostwald,

indicating incomplete ripening prior to the preservation of their shapes by supply-limited proportionate growth (Fig. 5 in Kile et al. 2000).

The Ostwald and transitional CSD shapes were readily crystallized in the laboratory where they formed for calcite by the rapid mixing of concentrated calcium and carbonate solutions (Kile et al. 2000). However, such environmental conditions are rare in nature. The Ostwald shape has been found for garnets in metamorphic rock by Miyazaki (1991). Carlson (1999) objected to this interpretation because the surface energy driving force for the ripening of such large porphyroblasts would be negligible. Carlson correctly reasoned that ripening should not be effective for crystals larger than a fraction of a μm. However, as was discussed, the Oswald distributions likely formed from extremely small crystals during and immediately after nucleation. These shapes then were preserved for the garnets during supply-limited proportionate growth.

An entire sequence of CSD shapes, from Ostwald to transitional to lognormal, has been found on Mars for hematite concretions (Martian blueberries; Figs. 2 and 3 in Eberl 2022). Concretion diameters were measured from photographs taken during a traverse by the Opportunity rover. This set of distribution shapes indicates differences in initial relative levels of groundwater supersaturation with respect to hematite solubility (see Fig. 6 in Kile et al. 2000 for analogous calcite experiments). Concretions likely precipitated from hydrothermal solutions that were generated suddenly by bolide impact on groundwater or permafrost (Eberl 2022). Iron for the hematite may have come from the bolide.

There is another kind of ripening, other than Ostwald, during which crystals dissolve randomly with respect to size, thereby supplying nutrients for other crystals to grow. During such supply-limited random ripening (also termed non-Ostwald ripening) something other than

specific surface area influences solubility. For example, some crystals could be less stable due to lattice strain, polytype, or because they are located in hotspots. Assuming that the less stable crystals disappear completely, the initial CSD shape (β^2) remains constant as mean size increases (Fig.11 in Eberl et al. 1998), thereby mimicking supply-limited growth; but this process differs because it occurs in a closed system (here defined as a system in which nutrients for growth come from the dissolution of the crystals themselves), and because a large amount of material passes through solution for a small increase in mean size. It is not known if random ripening is an important growth mechanism in nature because its CSD does not have a distinctive shape of its own. Evidence for such ripening has been noted experimentally in isotopic studies of the growth of Fisher calcite crystals treated hydrothermally in a closed system at 500° C for various lengths of time (Figs. 18 and 19 in Eberl et al. 1998).

Mineral CSDs may have other shapes. For example, samples that have undergone several nucleation events can be composed of multiple lognormal distributions (Fig. 2C in Kile et al. 2000). These distributions can be decomposed into their component lognormal CSDs by fitting them with appropriate means and variances using Equation 1. In addition, CSD shapes that have undergone mixing or winnowing by sediment transportation can be recognized by the relation between α and β^2, the values for which may lie outside a field expected for *in situ* crystal growth, as was demonstrated for the clay mineral illite in Yukon River sediments (Fig. 18B in Eberl 2004). In a like manner, the reaction path for illite crystals can be ascertained from their thickness distribution shapes by plotting distribution parameters onto an α vs. β^2 diagram, as was shown for illite crystals from the San Juan Mountains, Colorado (Figs. 6 and 7 in Bove et al. 2002).

ORIGIN OF PROPORTIONATE GROWTH

CSDs may increase in mean size by proportionate growth or by constant growth (Eberl et al. 2002a). The latter growth law, which is expressed $X_{(j+1)} = X_j + k$, often is assumed in modeling (e.g., population balance modeling; McCabe's ΔL law; JMAK equation), but rarely is found in nature. Growth experiments with centimeter size K-alum crystals having a variety of initial sizes indicate that, for such large crystals, proportionate growth occurs in stirred systems, whereas constant growth occurs in systems that are not stirred (Figs. 1 and 2 in Kile and Eberl 2003). Thus, the advective supply of nutrients to crystals favors proportionate growth, whereas diffusion in still solutions leads to constant growth. The reason for this behavior is attributed to a nutrient depleted boundary layer in solution next to a crystal. This layer is progressively thinned by the greater velocity necessary for a solution to contour around larger crystals, thereby tending to increase growth rate based on crystal diameter, as has been modeled by Stefan-Kharicha et al. (2020).

A contrary result was found during the experimental nucleation and growth of fine (28 μm mean) calcite crystals (Fig. 3 in Kile and Eberl 2003). They exhibited proportionate growth by retaining a lognormal CSD for both stirred and unstirred systems, an effect attributed to to their small size and to solution movement during initial mixing or to visually unobserved convection and/or Brownian motion (Kile the al. 2000). However, calcite CSDs did show the narrowing effect expected for constant growth when grown from concentrated solutions in a silica gel-filled column (Kile and Eberl 2003). Silica gel was used to minimize advection and increase nutrient supply by diffusion. These calcite crystals grew to a mean diameter of about 310 μm, and had a very small variance of 0.02. An initial Ostwald distribution shape and variance ($\beta^2 = 0.07$) was recovered by subtracting a constant 140 μm from each crystal diameter, indicating that constant

growth began to alter an Ostwald distribution shape at a mean diameter of about 170 μm (Fig. 4c in Kile and Eberl 2003).

Two examples of constant growth were discovered in natural flow-restricted environments (Kile et al. 2000). Calcite CSDs within a molar tooth structure (Proterozoic Belt Supergroup, Western Montana, USA), having a mean size of 13 μm and a variance of 0.02, started constant growth at 7.5 μm from an initial Ostwald distribution shape (Fig. 5 in Kile and Eberl 2003). Possible greigite crystals, found in a diatom test in Pyramid Lake, NV, also may have undergone some constant growth that deformed an initial Ostwald CSD (Fig. 6 in Kile and Eberl 2003).

There may be a practical application for these observations. If one wants to create a CSD containing uniform sizes (for example, a non-scoring abrasive or a congruently dissolving drug), one could encourage the initial formation of an Ostwald CSD by nucleation at large supersaturation, followed by constant growth in an immobile solution which would further decrease variance (Eberl et al. 2002b). It may also be possible to encourage a narrowing of CSDs through rapid stirring or flushing, whereby the flow of solution around crystals is fast enough to be minimally affected by crystal diameters.

IMPLICATIONS

The LPE, and the related volume constrained LPE, offer a concise and simple explanation for some of the baffling features concerning crystal growth, including size dependent growth, crystal growth dispersion, the common lognormal shape, and the narrow range of variance for each of the three basic types of CSDs (Fig. 7 in Kile et al. 2000). The equation also indicates that growth depends on the incorporation of nanoparticles rather than single atoms, a prediction that accords with electron micrograph evidence mentioned previously.

A random number lies at the heart of this equation; but what are the consequences of accepting randomness? As was discussed, randomness means that the growth rate of individual crystals can not be calculated precisely, but only the distribution shape can be predicted. In an analogy to crystal growth, randomness also appears in the foundations of quantum mechanics. The double slit experiment indicates that one can not calculate (based on the Schrödinger equation) the precise location of an electron fired through double slits onto a fluorescent screen, but one can only predict the shape of the distribution of a large number of electrons striking the screen. Likewise, one can not predict the moment for the radioactive decay of an individual atom, but only the decay rate for a large group of atoms. Stochastic models also are used to model chemical reactions (Gillespie 2007). In fact, many natural systems likely have such built-in randomness (Mann 1970), especially if they express a lognormal distribution. The presence of a random component means that experimental results are not precisely reproducible no matter how much care is taken. However, on the positive side, the presence of randomness frees us from a completely deterministic world view.

ACKNOWLEDGMENTS

I thank Manny Knill and Lynda Williams for their substantial comments on the initial manuscript. I also thank my former coauthors, especially Dan Kile for his excellent experimental work. Thanks also to Alain Baronnet who introduced the author to the science of CSDs during a lecture in Paris many years ago. I apologize to scientists who were misled by mistaken notions concerning crystal growth published in Eberl et al. (1988, 1990). I would like to acknowledge pioneering papers on the use of CSDs in geology by Marsh (1988), Cashman and Ferry (1988), and Cashman and Marsh (1988), papers that were partly based on investigations of crystal growth in continuous-flow industrial crystallizers by Randolph and

316 Larson (1971). Such geological studies generally assume a constant-rate growth law in a
317 population balance equation, whereas the present paper emphasizes a different approach. I am
318 deeply grateful to the US Geological Survey for its support of this research prior to my
319 retirement.

320 ## REFERENCES CITED

321 Badino, G.V., Ferreira, A., Forti, P., Giovani, P., Giulivo, I., Infante, G., Lo Mastro, F., Sanna,
322 L., and Tedeschi, R. (2009) The Naica caves survey. Fifteenth International Congress of
323 Speleology At: Kerrville, Texas, 1764-17869.

324 Bove, D.J., Eberl, D.D., McCarty, D.K., and Meeker, G.P. (2002) Characterization and modeling
325 of illite crystal particles and growth mechanisms in a zoned hydrothermal deposit, Lake
326 City, Colorado. American Mineralogist, 87, 1546-1556.

327 Carlson, W. (1999) The case against Ostwald ripening of porphyroblasts. Canadian Mineralogist,
328 37, 403-413.

329 Cashman, K.V., and Ferry, J.M. (1988) Crystal size distribution (CSD) in rocks and the kinetics
330 and dynamics of crystallization iii. Metamorphic crystallization. Contributions to
331 Mineralogy and Petrology, 99, 401-405.

332 Cashman, K.V., and Marsh, B.D. (1988) Crystal size distribution (CSD) in rocks and the kinetics
333 and dynamics of crystallization ii. Makaopuhi lava lake. Contributions to Mineralogy and
334 Petrology, 99, 292-305.

335 De Yoreo, J.J., Gilbert, P.U.P.A., Sommerdijk, N.A.J.M., Penn, R.L., Whitelam, S., Joester, D.,
336 Zhang, H., Rimer, J.D., Navrotsky, A., Banfield, J.F., Wallace, A.F., Michel, F.M.,
337 Meldrum, F.C., Cölfen, H., and Dove, P.M. (2015) Crystallization by particle attachment

in synthetic, biogenic, and geologic environments. Science, 349, print extended abstract at pg. 498, online at aaa6760 DOI: 10.1126/science.aaa6760.

Eberl, D.D. (2004) Quantitative mineralogy of the Yukon River system: Changes with reach and season, and determining sediment provenance. American Mineralogist, 89, 1784-1794.

Eberl, D.D. (2022) On the formation of Martian blueberries. American Mineralogist, 107, 153-155.

Eberl, D.D., and Srodon, J. (1988) Ostwald ripening and interparticle-diffraction effects for illite crystals. American Mineralogist, 73, 1335-1345.

Eberl, D.D., Srodon, J., Kralik, M., Taylor, B.E., and Peterman, Z.E. (1990) Ostwald ripening of clays and metamorphic minerals. Science, 248, 474-477.

Eberl, D.D., Drits, V.A., and Srodon, J. (1998) Deducing crystal growth mechanisms for minerals from the shapes of crystal size distributions. American Journal of Science, 298, 499–533.

Eberl, D.D., Drits, V.A., and Srodon, J. (2000) User's guide to GALOPER --: a program for simulating the shapes of crystal size distributions—and associated programs: U.S. Geological Survey Open-File Report, OF 00-505, 44 pp.

Eberl, D.D., Kile, D.E., and Drits, V.A. (2002a) On geological interpretations of crystal size distributions: Constant vs. proportionate growth. American Mineralogist, 87, 1235–1241.

Eberl, D.D., Kile, D.E., and Hoch, A.R. (2002b) Crystallization of powders having uniform particle sizes by Ostwald ripening at large levels of supersaturation. U.S. Patent 6,379,459, April 30, 2002.

359 Gillespie, D.T. (2007) Stochastic simulation of chemical kinetics. Annual Review of Physical
360 Chemistry, 58, 35-55.

361 Ivanov, V.K., Fedorov, P.P., Baranchikov, A.Y., and Osiko, V.V. (2014) Oriented attachment of
362 particles: 100 years of investigations of non-classical crystal growth. Russian Chemical
363 Reviews, 83, 1204-1222.

364 Kile, D.E., and Eberl, D.D. (1999) Crystal growth mechanisms in miarolitic cavities of the Lake
365 George ring and vicinity, Colorado. American Mineralogist, 84, 718-724.

366 Kile, D.E., and Eberl, D.D. (2003) On the origin of size-dependent and size-independent crystal
367 growth: Influence of advection and diffusion. American Mineralogist, 88, 1514-1521.

368 Kile, D.E., Eberl, D.D., Hoch, A.R., and Reddy, M.M. (2000) An assessment of calcite crystal
369 growth mechanisms based on crystal size distributions. Geochimica et Cosmochimica
370 Acta, 64, 2937-2950.

371 Koch, A.L. (1966) The logarithm in biology 1. Mechanisms generating the lognormal
372 distribution exactly. Journal of Theoretical Biology, 12, 251-268.

373 Lifshitz, I.M., and Slyozov, V.V. (1961) The kinetics of precipitation from supersaturated solid
374 solutions. Journal of Physics and Chemistry of Solids, 19, 35-50.

375 Markworth, A.J. (1970) The kinetic behavior of precipitate particles under Ostwald ripening
376 conditions. Metallography, 3, 197-208.

377 Mann, C.J. (1970) Randomness in nature. Geological Society of America Bulletin, 81, 95-104.

378 Marsh, B.D. (1988) Crystal size distribution (CSD) in rocks and the kinetics and dynamics of
379 crystallization. 1. Theory. Contributions to Mineralogy and Petrology, 99, 277-291.

Miyazaki, K. (1971) Ostwald ripening of garnet in high P/T metamorphic rocks. Contributions to Mineralogy and Petrology, 108, 118-128.

Randolph, A.D., and Larson, M.A. (1971) Theory of Particulate Processes: Analysis and Techniques of Continuous Crystallization, 1st Edition, 251 p. Academic Press, New York.

Stefan-Kharicha, M., Kharicha, A., Zaidat, K., Reiss, G., Essl, W., Goodwin, F., Wu, M., Ludwig, A., and Mugraue, C. (2020) Impact of hydrodynamics on growth and morphology of faceted crystals. Journal of Crystal Growth, 541, 1-11.

Wagner, C. (1961) Theorie der alterung von niederschlägen durch umlösen (Ostwald reifung). Zeitschrift Fuer Elektrochimie, 65, 581–591 (in German).

This is the peer-reviewed, final accepted version for American Mineralogist, published by the Mineralogical Society of America.
The published version is subject to change. Cite as Authors (Year) Title. American Mineralogist, in press.
DOI: https://doi.org/10.2138/am-2022-8851. http://www.minsocam.org/

Figures

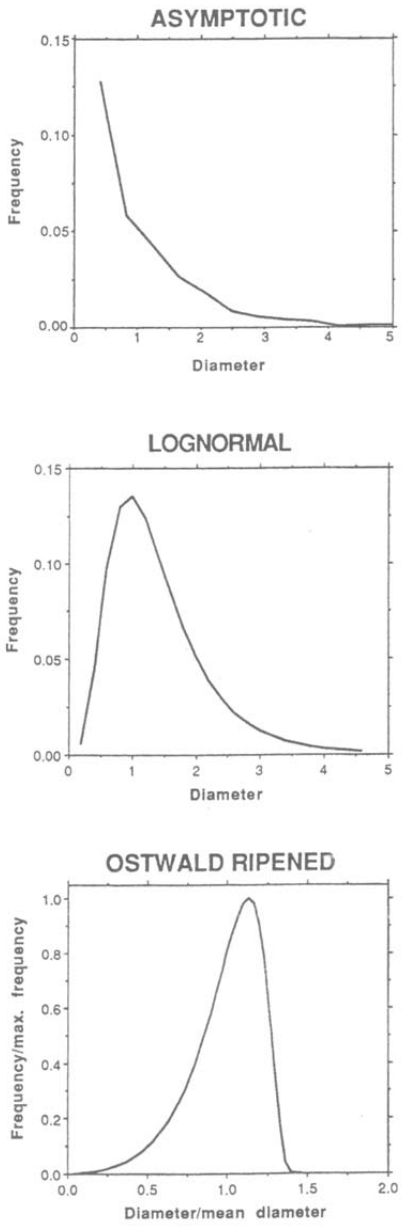

Figure 1. The three fundamental shapes for crystal size distributions. All have been produced in synthesis experiments, by calculation, and have been found in nature. This figure is from Kile et al. (2000).

SUPPLEMENTARY MATERIAL FOR THE PAPER:

Crystal Growth According to the Law of Proportionate Effect

by D. D. Eberl

(Figures can be expanded for easier viewing)

Badino, G., Ferreira, A., Forti, P., Giovani, P., Giulivo, I, Infanti3, G., Lo Mastro, F., Sanna, L., and Tedeschi, R. (2009) The Nasca caves survey. Fifteenth International Congress of Speleology At: Kerrville, Texas, 1764-17869.

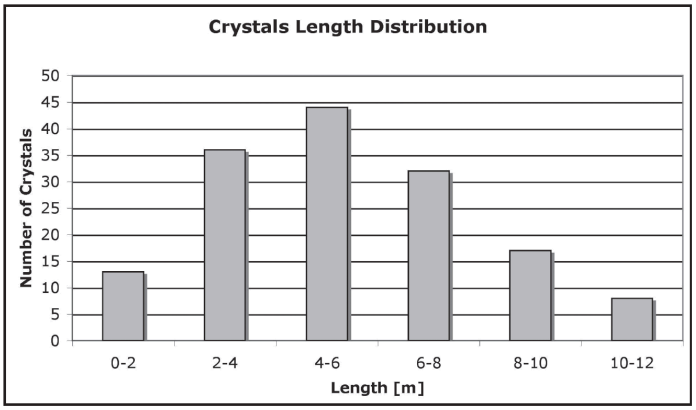

Figure 5: Cristales, distribution of crystals lengths.

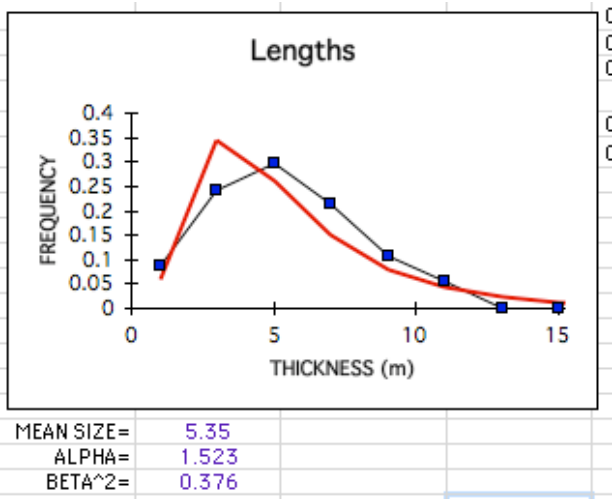

MEAN SIZE=	5.35
ALPHA=	1.523
BETA^2=	0.376

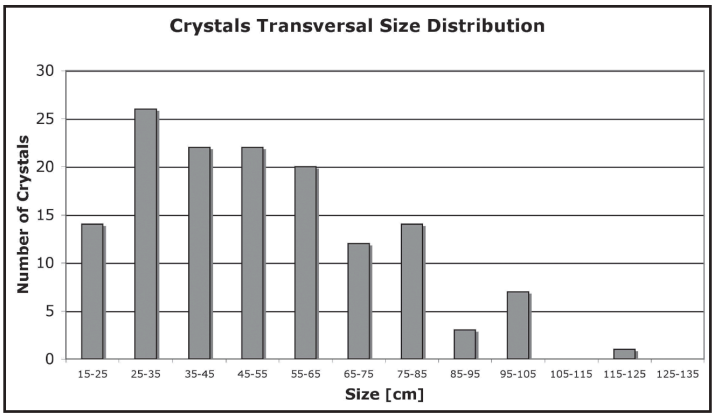

Figure 7: Cristales, distribution of crystals transversal sizes.

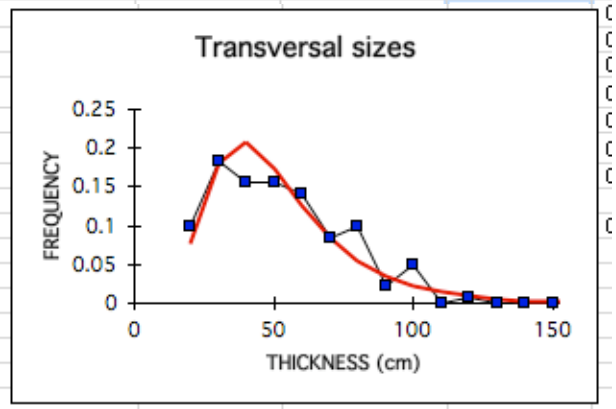

MEAN SIZE=	51.7
ALPHA=	3.846
BETA^2=	0.208

Both of the above distributions pass the Kolmogorov-Smirnov test for lognormal shape (the red curves) at the > 10% level, the most significant level in the tables.

Bove, D., Eberl, D., McCarty, D., and Meeker, G. (2002) Characterization and modeling of illite crystal particles and growth mechanisms in a zoned hydrothermal deposit, Lake City, Colorado. American Mineralogist, 87, 1546-1556.

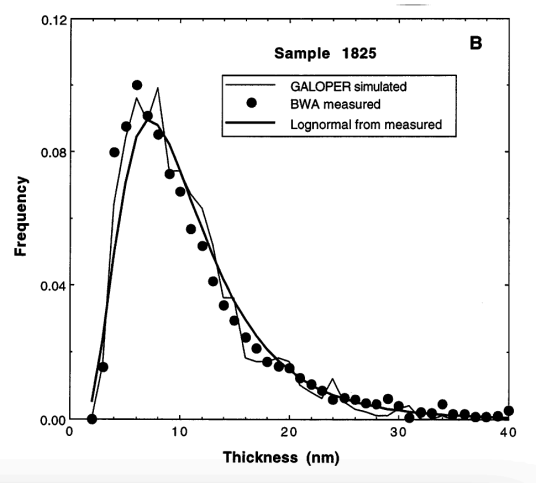

Figure 5b. Lognormal shape for illite crystal thicknesses from Red Mountain, Colorado. Alpha = 2.24, and beta^2 = 0.32.

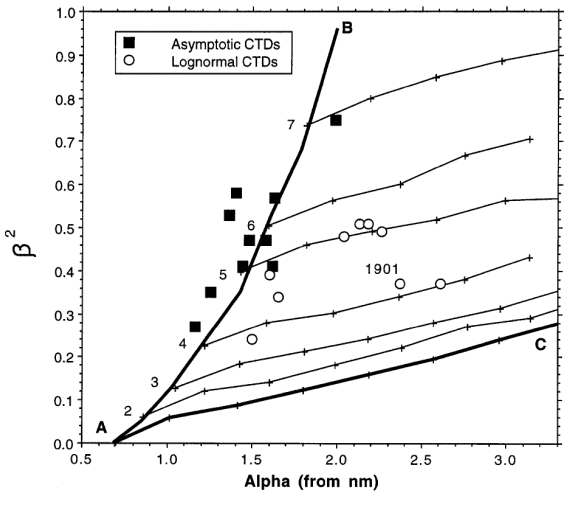

FIGURE 6. Alpha-β^2 diagram showing these parameters for illite crystallite thickness distributions having the two basic shapes. See text for explanation.

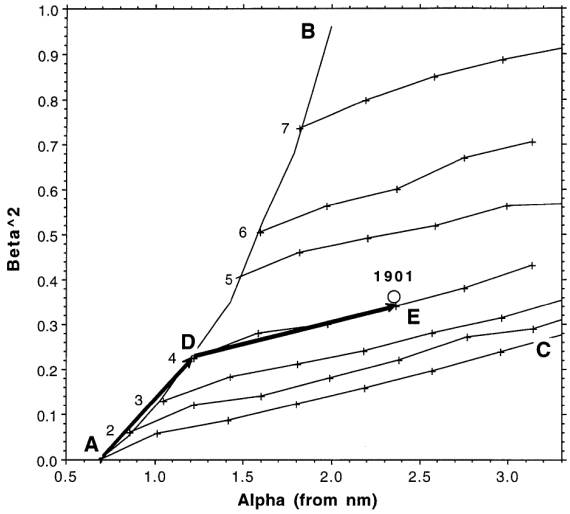

FIGURE 7. Alpha-β^2 digram showing the unique reaction path (A-D-E) that simulates the shape of the crystallite thickness distribution for sample 1901.

De Yoreo, J.J., Gilbert, P.U.P.A., Sommerdijk, N.A.J.M., Penn, R.L., Whitelam, S., Joester, D., Zhang, H., Rimer, J.D., Navrotsky, A., Banfield, J.F., Wallace, A.F., Michel, F.M., Meldrum, F.C., Cölfen, H., and Dove, P.M. (2015) Crystallization by particle attachment in synthetic, biogenic, and geologic environments. Science, 349, print extended abstract at pg. 498, online at aaa6760 DOI: 10.1126/science.aaa6760.

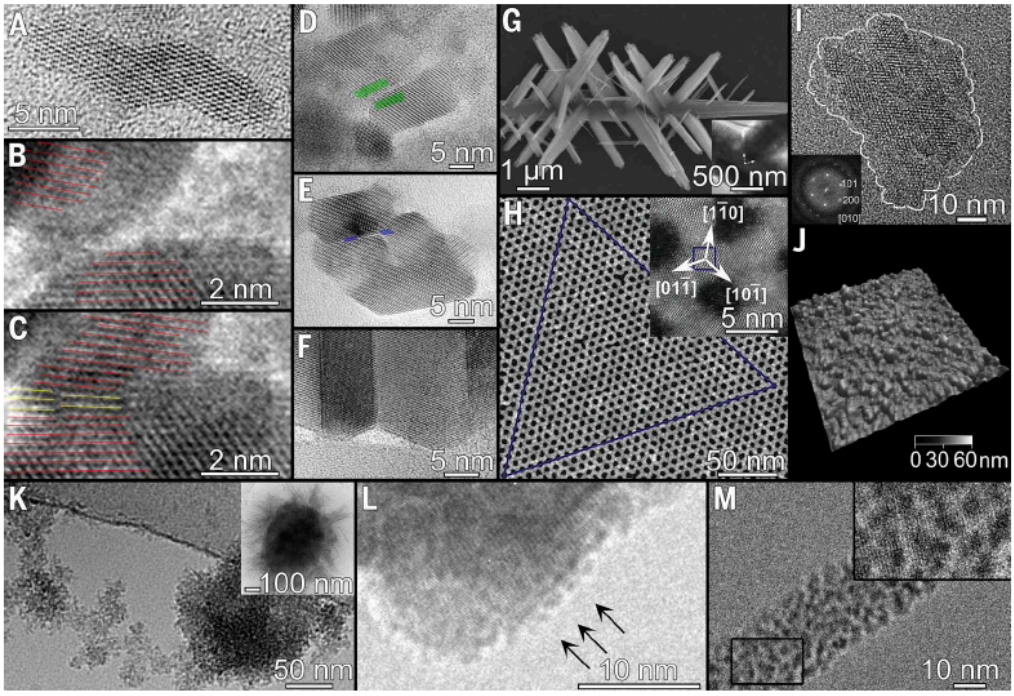

Fig. 2. Examples of inorganic crystals formed by CPA. (**A**) Nanoparticles of anatase (TiO_2) with perfect alignment after apparent attachment event with the *c* axis oriented along the long dimension of the aggregate (*116*). (**B** and **C**) Sequential in situ images showing oriented attachment of ferrihydrite with creation of an edge dislocation (yellow lines) and resulting tilt of lattice planes above and below the edge dislocation (red lines) (*27*, *30*). (**D** to **F**) TiO_2 nanocrystals showing defects incorporated through CPA, including (D) low-angle tilt boundaries, (E) screw dislocations, and (F) twin planes. In (E), the variations in contrast and slight shift in lattice fringe clarity and alignment indicate incorporation of defects. The blue lines highlight the orientation and shift in lattice fringe alignment to either side of the region that contains the dislocations; the bright-dark contrast is consistent with a dislocation having a screw component. (**G**) Branched nanowire of rutile (TiO_2), where each branch occurs on a set of twin boundaries (inset) (*60*). (**H**) Single-crystal honeycomb superlattice formed through oriented attachment of PbSe nanocrystals in an octahedral symmetry. The equilateral triangle shows the long-range ordering of the structure, and the inset shows the relationship of the crystalline axes with the superlattice pattern (*39*) (**I**) Cryo-TEM micrograph of a single zeolite nanoparticle (*117*). (**J**) Atomic force micrograph of a zeolite surface showing that its growth proceeds by attachment of silica nanoparticles (*28*). (**K**) Calcium phosphate prenucleation complexes aggregating to form amorphous calcium phosphate nanoparticles. (Inset) Amorphous calcium phosphate nanoparticle is replaced by outgrowths of calcium-deficient octacalcium phosphate (*5*). (**L**) Magnetite crystal growing through the accretion of disordered ferrihydrite-like nanoparticles (*57*). (**M**) Goethite mesocrystal formed by the assembly of nanocrystals shows lattice fringes that correspond to (021) planes (*62*).

Eberl, D. (2022) On the formation of Martian blueberries. American Mineralogist, 107, 153-155.

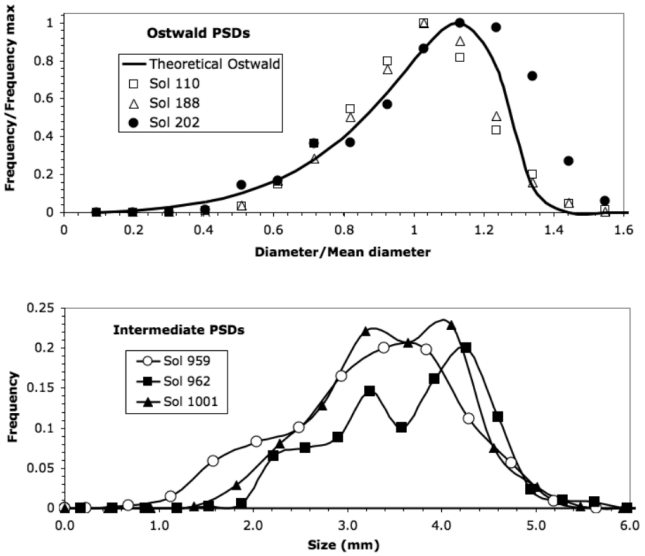

FIGURE 2. Changes in the shapes of particle size distributions as the rover neared Endurance Crater rim (upper) and Victoria Crater rim (lower), showing a change from the universal steady-state Ostwald-shaped reduced PSDs (upper) to transitional PSDs (lower). The original PSD data comes from Royer et al. (2008).

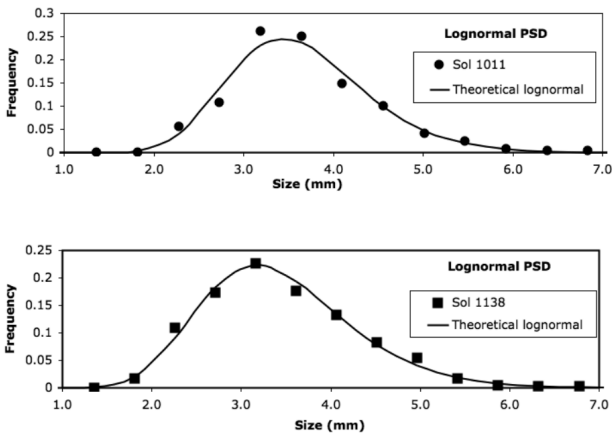

FIGURE 3. The two best examples of lognormal PSDs from Victoria Crater rim. The other four samples in this data set skew to the right, and pass the Kolmogorov-Smirnov statistical test for log normality: sol 1124 from 1 to 5%, sol 1071 from 5 to 10%, and sols 1113 and 1139 (and the two sols shown above) to the >10% level of confidence, the highest level in the tables. The original PSD data comes from Royer et al. (2008).

Eberl, D. (2004) Quantitative mineralogy of the Yukon River system: Changes with reach and season, and determining sediment provenance. American Mineralogist, 89, 1784-1794.

Figure 18B

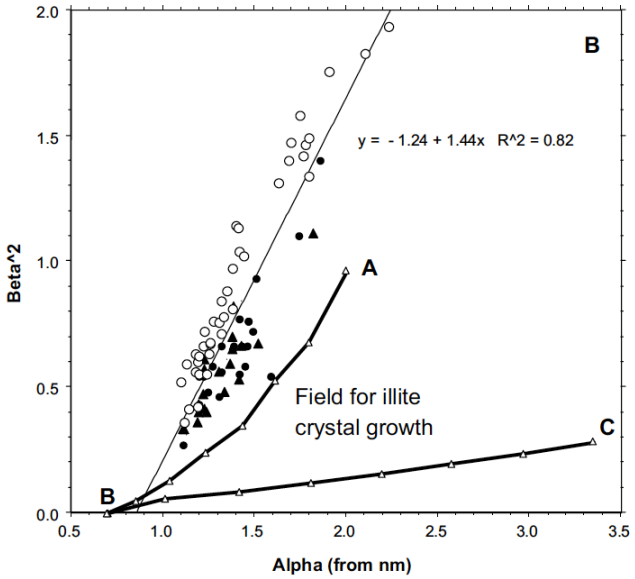

(see text). (**b**) Plot of α and β^2 values for crystallite size distributions for illites found in suspended sediments (open circles), Yukon River bed sediments (filled circles), and tributary bed sediments (filled triangles).

Eberl, D., Drits, V., and Srodon, J. (1998) Deducing crystal growth mechanisms for minerals from the shapes of crystal size distributions. American Journal of Science, 298, 499–533.

TABLE 2

Summary of crystal growth mechanisms and their characteristics

System	Growth Mechanism	CSD Shape	Comments
Open	Nucleation and growth with constant or accelerating nucleation rate.	Asymptotic.	β^2 increases exponentially with increase in α.
	Nucleation and growth with decaying nucleation rate.	Lognormal.	β^2 increases linearly with increase in α.
	Surface-controlled growth.	Lognormal.	β^2 increases linearly with increase in α.
	Supply-controlled growth.	Preserves shape of previous CSD.	β^2 remains constant with increase in α; therefore, steady-state reduced profiles.
Closed	Ostwald ripening (supply-controlled).	CSD becomes more symmetrical with increasing percentage of ripening, becomes negatively skewed, and eventually approaches universal steady-state reduced profile.	Distribution maximum moves to the right of theoretical lognormal curve. Generally, β^2 decreases with increase in α. Universal steady-state profile may not be reached.
	Random ripening (supply-controlled). Also termed non-Ostwald or kinetic ripening.	Preserves shape of previous CSD.	A large amount of material passes through solution for a small increase in mean size. β^2 remains constant with increase in α; therefore steady-state reduced profiles.
	Agglomeration.	Can be pseudo-lognormal or multimodal, or have other shapes.	Very little material need pass through solution for a large increase in mean size. If most of the crystals are involved, β^2 may decrease; otherwise it may increase.

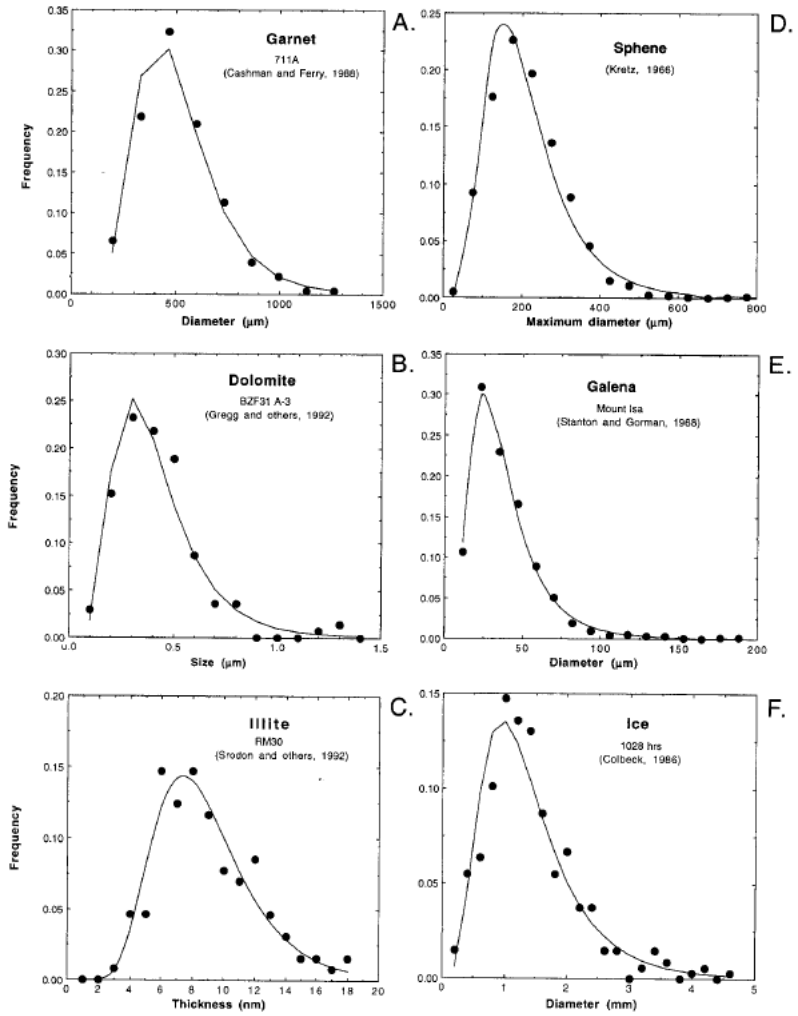

Fig. 1. Particle size data from the literature (points), with superimposed theoretical lognormal curves calculated from these data (solid lines).

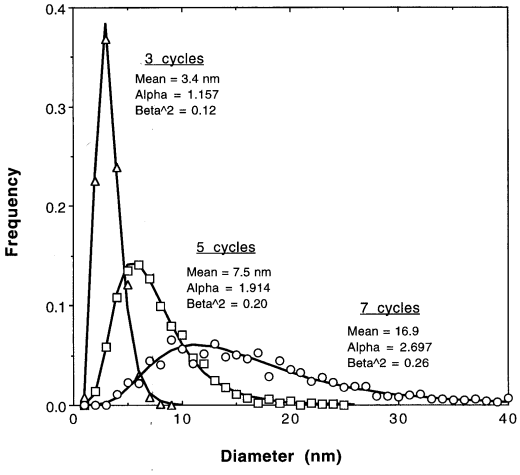

Fig. 2. GALOPER-calculated CSDs (symbols) for surface-controlled open system growth, using 3, 5, and 7 calculation cycles (eq 5) and an initial crystal diameter of 1 nm, compared with theoretical lognormal curves calculated from these data (solid lines).

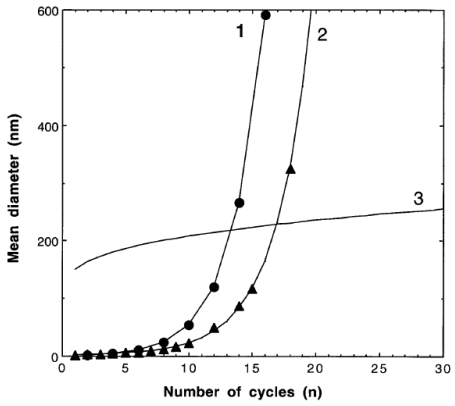

Fig. 3. Plots of rate equations (solid curves) for: (1) surface-controlled open system growth (eq 6 in text) starting with 2 nm crystals; (2) constant-rate nucleation and growth (eq 7 in text) starting with 2 nm crystals; and (3) supply-controlled growth (eq 9 in text) starting with a mean size of 100 nm and using k = 50. Epsilon was allowed to vary between 0 and 1 for all calculations (that is, ε = 0.5). The symbols represent GALOPER calculations for the corresponding growth mechanisms.

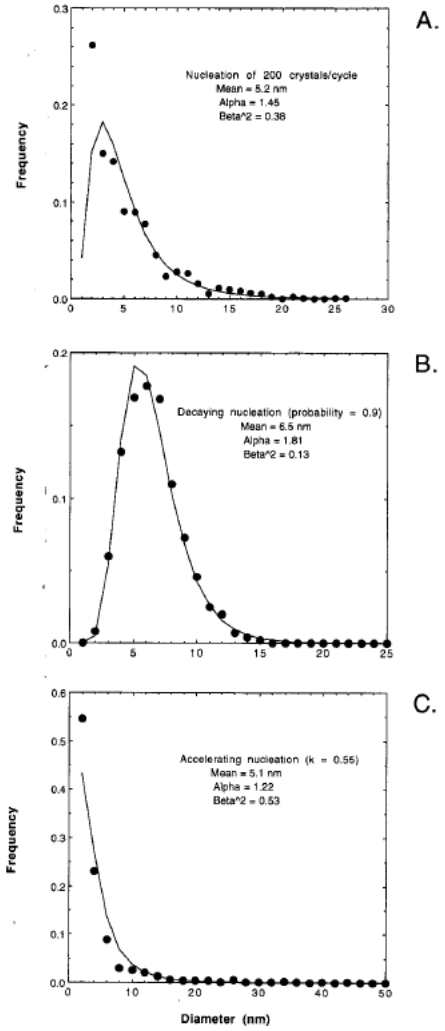

Fig. 4. GALOPER-calculated CSDs (points) for the continuous nucleation and growth mechanism assuming nucleation having: (A) a constant rate; (B) a decaying rate; and, (C) an accelerating rate. Critical nucleus size = 2.0 nm. The solid lines are lognormal fits to the data.

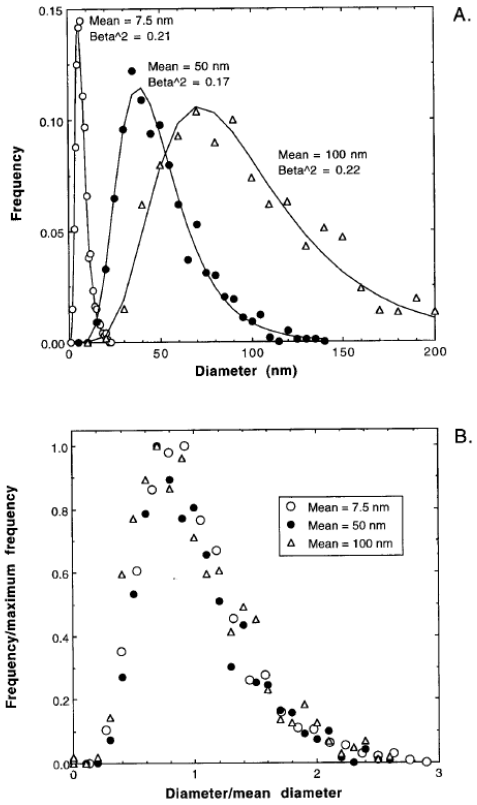

Fig. 6. GALOPER-calculated CSDs for supply-controlled open system overgrowth starting with a lognormal distribution. (A) = overgrowth starting with a lognormal CSD having a mean size of 7.5 nm; (B) = Steady-state reduced plot of CSDs in (A).

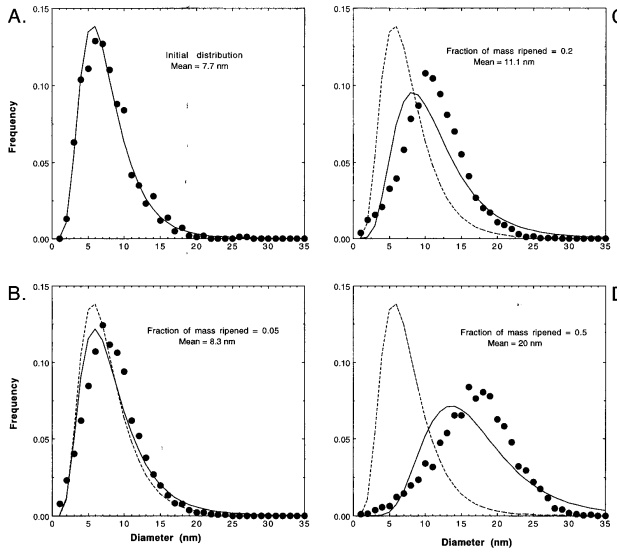

Fig. 8. GALOPER-calculated CSDs modified by Ostwald ripening. (A) = initial distribution; (B) = 5 percent of the initial mass has passed through solution once; (C) = 20 percent through solution; (D) = 50 percent through solution. The solid curves are theoretical lognormal curves calculated from the ripened CSDs (solid circles). The dashed curves are the shape of the original lognormal CSD in (A).

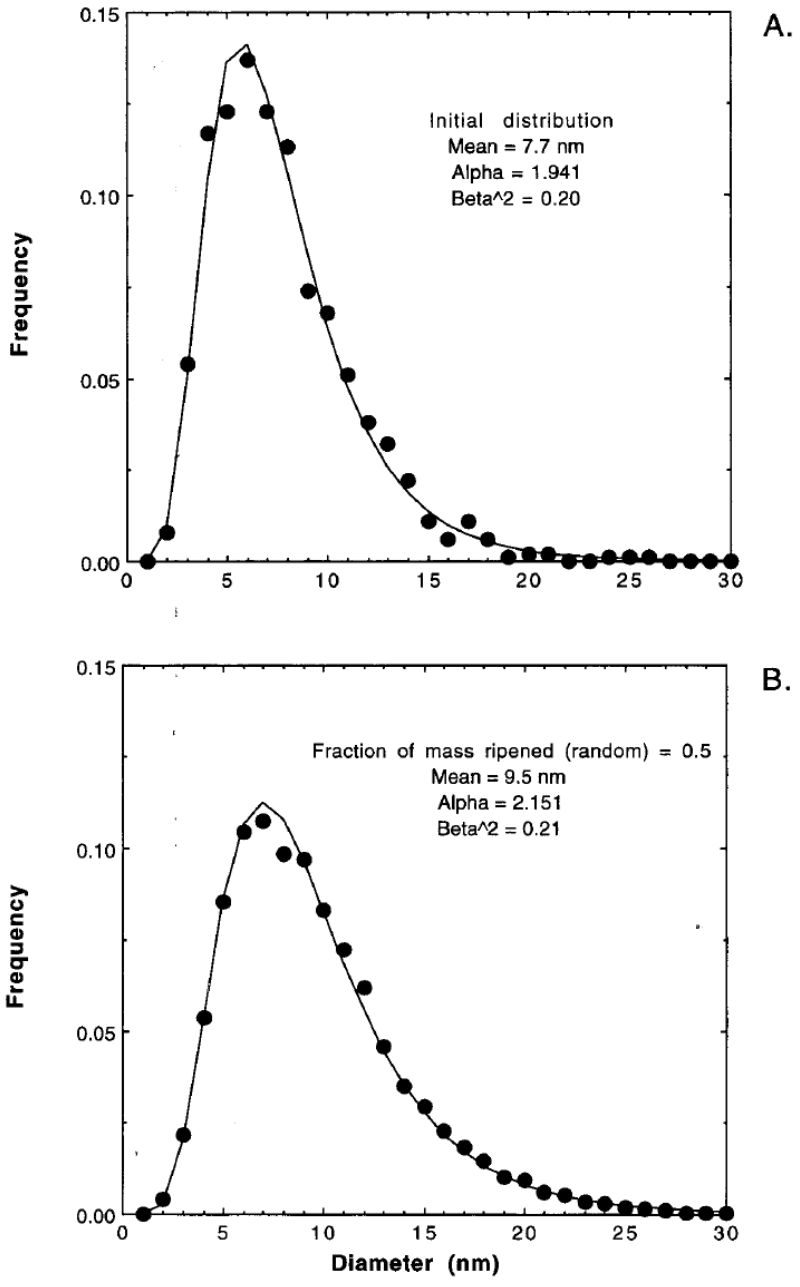

Fig. 11. GALOPER-calculated CSDs for random ripening. (A) = initial distribution; (B) = 50 percent of initial mass has passed through solution by supply-controlled random ripening. The solid circles are the calculated CSDs, and the solid lines are the theoretical lognormal curves.

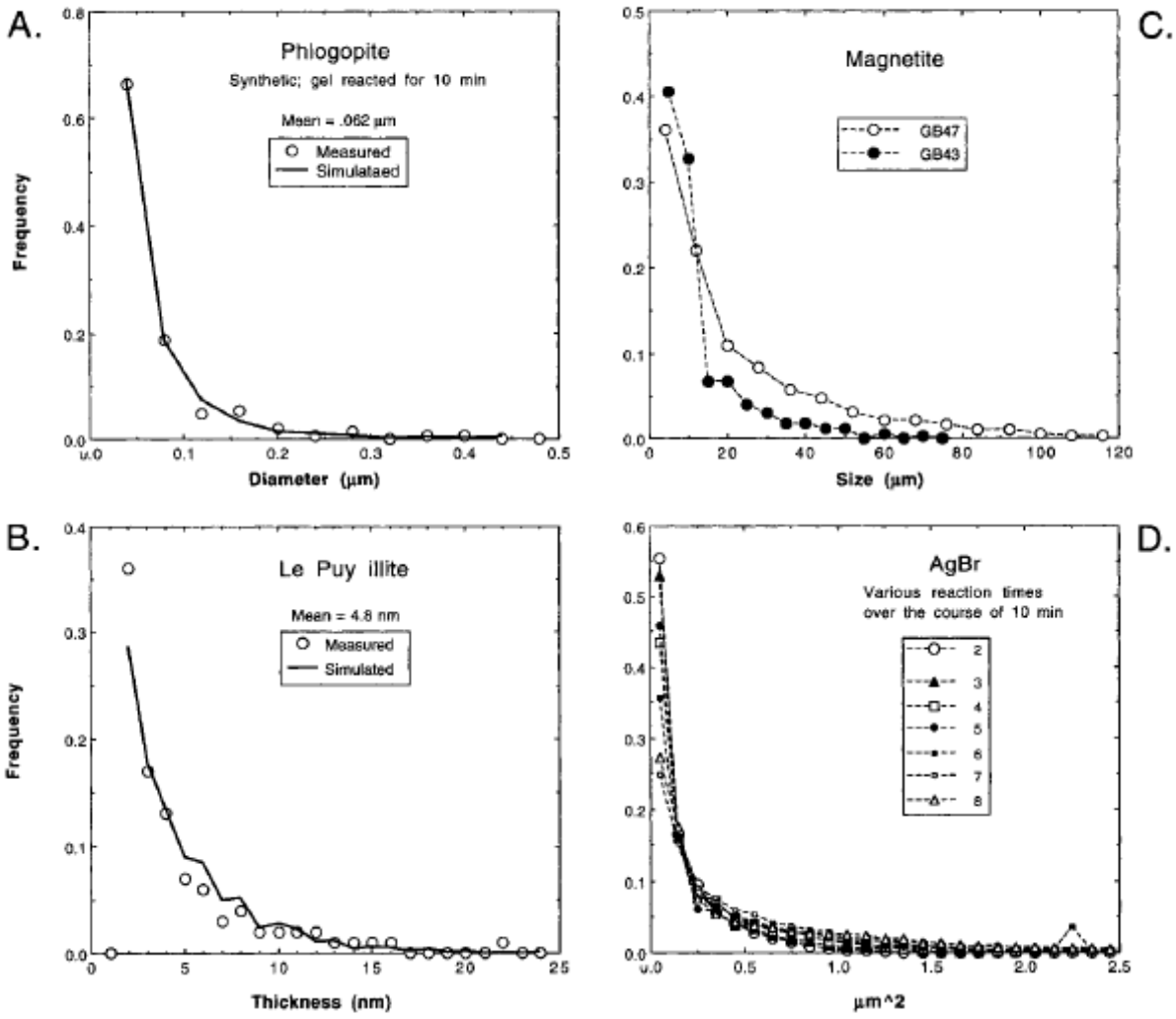

Fig. 13. Measured asymptotic-type CSDs for minerals, and GALOPER simulations. Shapes of CSDs are attributed to nucleation and growth with constant nucleation rate. (A) Phlogopite mean a-b diameters from Baronnet (1974 and personal communication), with GALOPER simulation (solid curve); (B) Le Puy illite thickness distribution, measured by the Bertaut-Warren-Averbach XRD method (Drits and others, 1998; Eberl and others, 1998), and GALOPER simulation (solid curve); (C) Magnetite from Cashman and Ferry (1988); AgBr data from Loveland and Trivelli (1947; L-1 precipitation, their fig. 7).

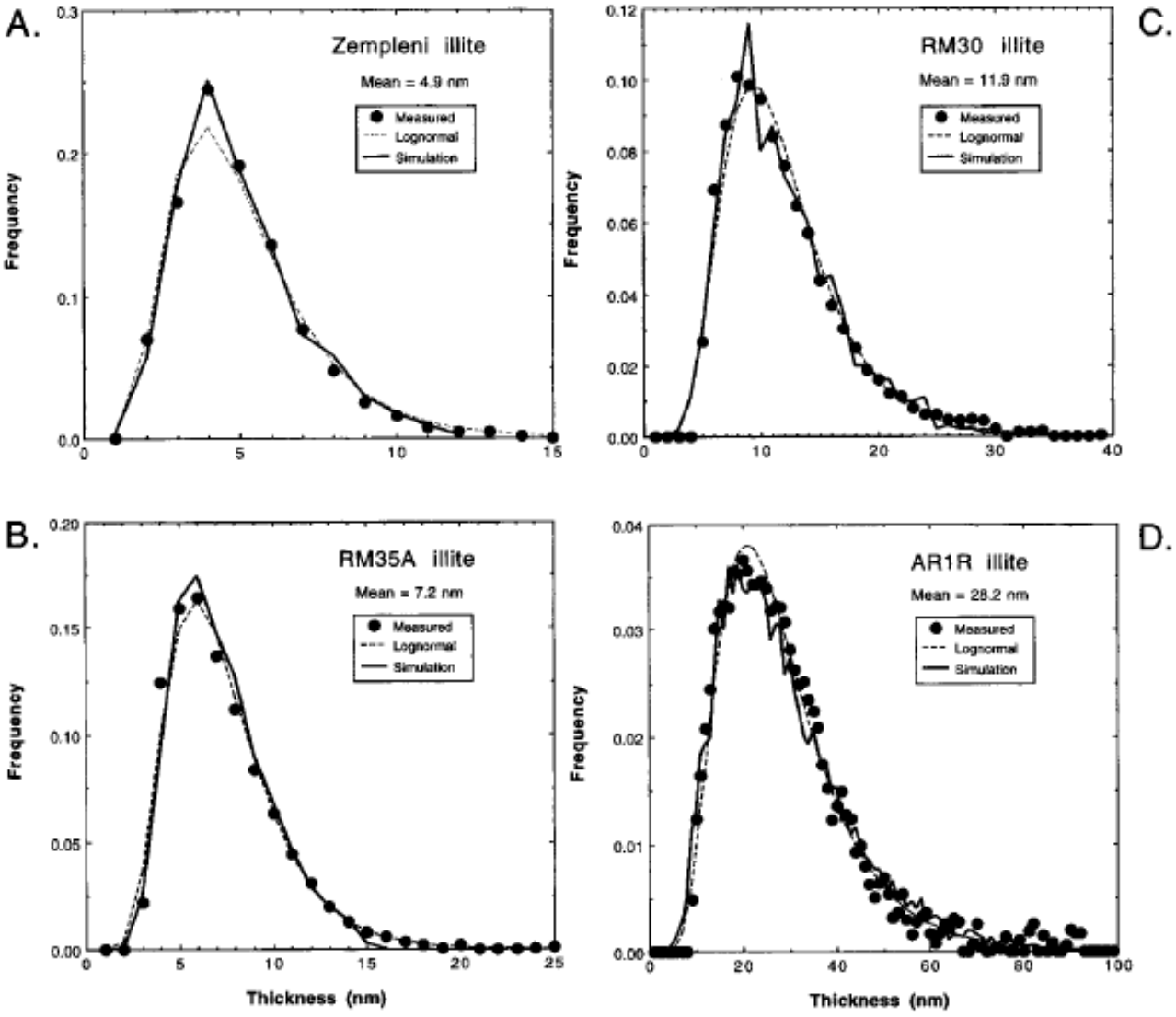

Fig. 15. Fundamental illite crystal thickness distributions for hydrothermal illites, measured by the authors by X-ray diffraction (Drits and others, 1998; Eberl and others, 1998). Points = measured distributions; dashed lines = lognormal curves calculated from the measurements; solid lines = GALOPER simulations. For information on the samples: (A) (Viczián, 1997); (B, C, and D) (Eberl and others, 1987).

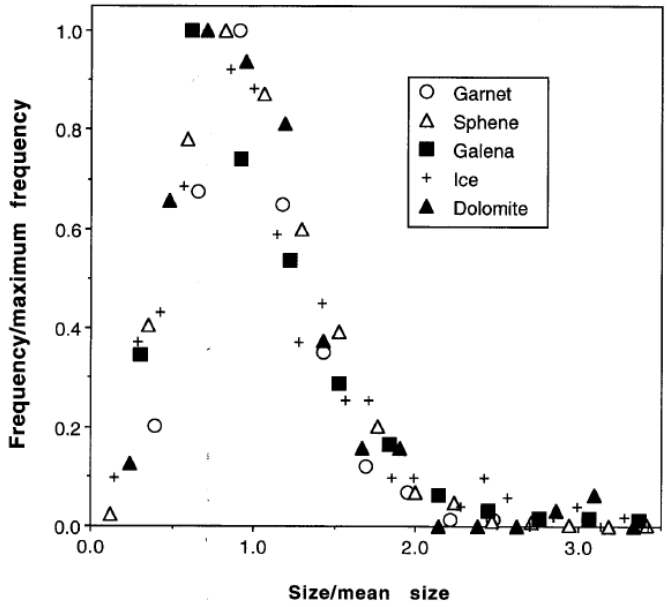

Fig. 16. Reduced CSDs calculated for minerals in figure 1, demonstrating steady-state shape.

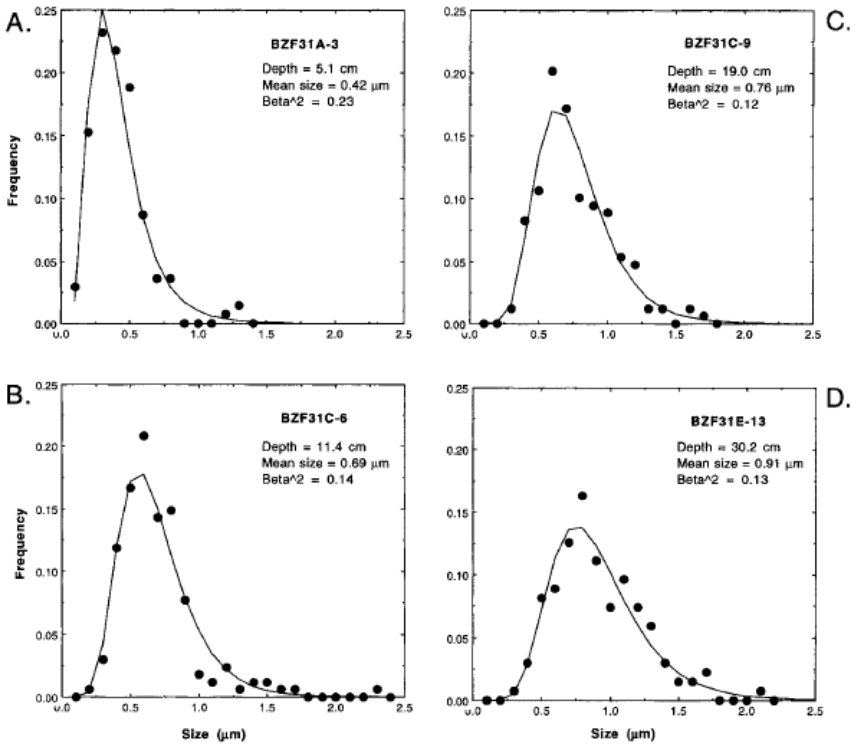

Fig. 17. Measured CSDs (symbols) compared with theoretical lognormal curves (solid lines) for dolomite CSDs collected at various depths from crusts from the bottom of Ambergris Cay, Belize (Gregg and others, 1992, and personal communication).

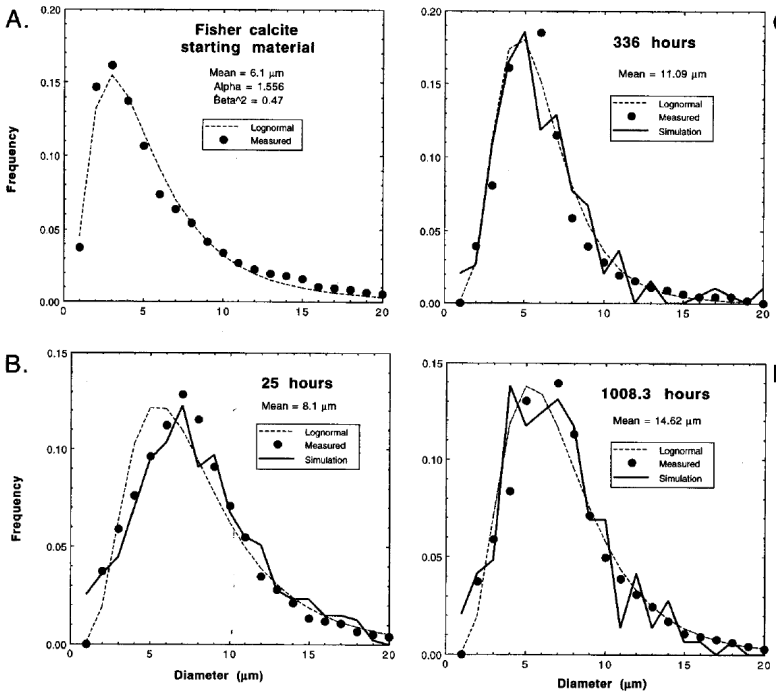

Fig. 18. CSDs (from figs. 44 and 45 in Chai, ms) from calcite ripening experiments compared with theoretical lognormal (dashed curves) and GALOPER simulations (solid curves). The initial Fisher calcite was ripened at 500°C and 2 kb for different lengths of time.

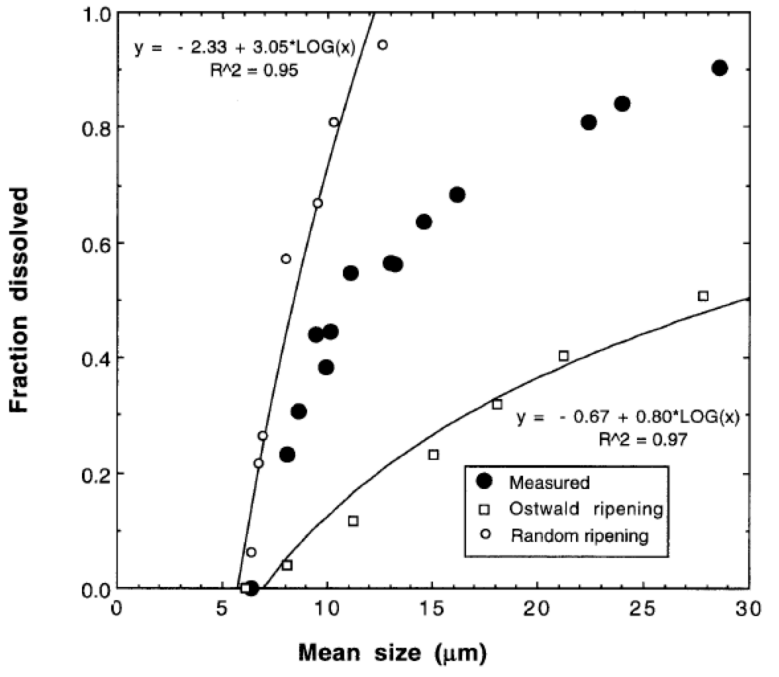

Fig. 19. Fraction dissolved (from oxygen isotope measurements) versus increase in mean crystal size for calcite ripening experiments, compared with theoretical, GALOPER-calculated curves for random ripening (upper curve) and Ostwald ripening (lower curve). Data from table 5 in Chai, ms).

Equation 8:

Supply-controlled growth in the open system.–One can imagine an open system in which the rate of crystal growth is controlled by the rate of nutrient supply rather than by the rate at which the crystal surface can grow in an infinite reservoir of nutrients. For example, the supply may be slowed by diffusion or by the rate of dissolution of an unstable phase that is a nutrient source, or crystals may grow so large that supply can not keep up with the exponentially increasing demand for nutrients required by LPE growth. This situation is simulated in GALOPER by specifying the total increase in volume that 1001 crystals are permitted ($\Sigma\Delta V_a$) during each cycle of eq (5). The crystals first are allowed to grow freely during a calculation cycle according to eq (5). Next the growth volume for that cycle for each crystal is calculated ($\Delta V_{j,LPE}$), and the growth volumes for all crystals are summed ($\Sigma\Delta V_{j,LPE}$). The unconstrained growth volume for each crystal then is reduced proportionately by the ratio of allowed volume to unconstrained growth volume:

$$\Delta V_j = (\Delta V_{j,LPE})\frac{\Sigma\Delta V_a}{\Sigma\Delta V_{j,LPE}}. \tag{8}$$

The corrected growth volume for each crystal (ΔV_j) is added to the previous volume of the crystal, and a new diameter for each crystal for that growth cycle is then calculated from the equation for the volume of a sphere. The calculation is repeated for each growth cycle. Therefore, during this type of growth the LPE is still the growth law, but growth is limited proportionately by supply.

Equation 10:

2. For diffusion-controlled ripening, the instantaneous rate at which a crystal changes size is given by:

$$\frac{dr}{dt} = \frac{K}{r}\left(\frac{1}{r^*} - \frac{1}{r}\right), \tag{10}$$

where r = the crystal radius, t = time (or calculation cycles), r* = the critical radius, which is equal to the mean radius ($\bar{r}$), and K is a constant (see app. 2).

Equation A20:

A remarkable feature of surface- and supply-controlled Ostwald ripening is the evolution of the crystal size distribution with the passage of time. It was shown by Lifshitz and Slyozov (1961) and Wagner (1961) that at large time this distribution can be approximated by certain universal functions that develop irrespective of the initial CSD. For example, in the case of supply-controlled crystal growth this function has the form:

$$f(r, t) = \text{Const}\frac{(t^{-4/3})u^2}{(3 - 2u)^{11/3}(3 + u)^{7/3}}\exp\left(\frac{3}{2u - 3}\right), \tag{A20}$$

where $u = r/\bar{r} = r/r^*$. As can be seen in figure 9A, normalized f(r, t) has an asymptotic profile with two characteristic features: (A) this function is equal or very close to zero at $u > 3/2$ or $r > (3/2)\bar{r}$; (B) it has a left-hand skewed distribution of crystal sizes.

Eberl, D., Kile, D., and Drits, V. (2002a) On geological interpretations of crystal size distributions: Constant vs. proportionate growth. American Mineralogist, 87, 1235–1241.

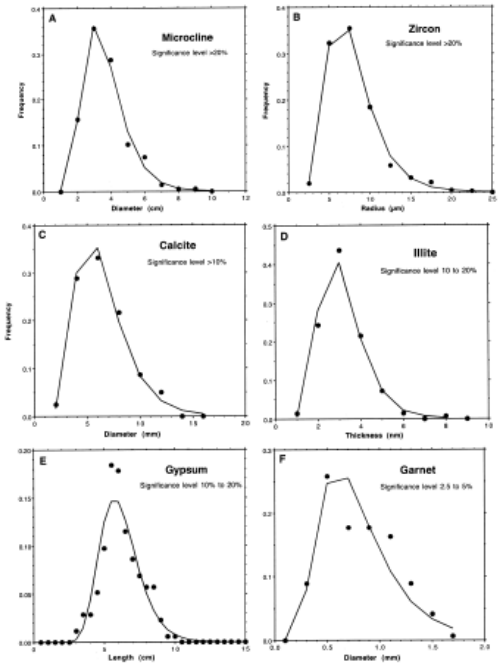

FIGURE 1. CSDs (solid circles) and lognormal fits (lines) with significance levels for chi-square test between the two. (A) Microcline, 1989 (Kile and Eberl 1999); (B) Zircon B, L total (Nemchin et al. 2001); (C) Calcite, SE Colorado (Kile et al. 2000); (D) Illite, Zampleni (Srodoń et al. 2000); (E) Gypsum from Jet, Oklahoma (this paper); (F) Garnet, Specimen 2 (Krotz 1966). Only the zircon CSD measurement (Fig. 1B) possibly is subject to stereological problems because it was measured from thin section.

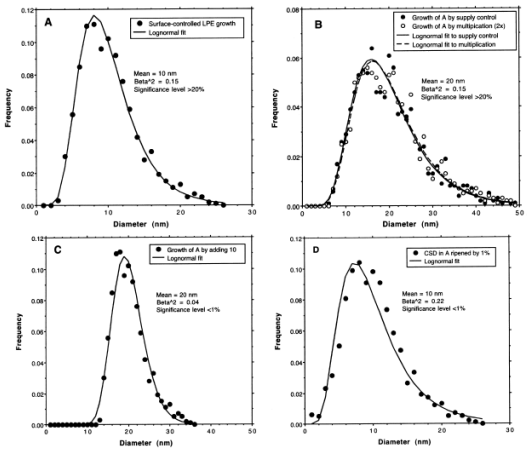

FIGURE 2. The effect of growth mechanisms on the shape of a lognormal CSD. (A) Initial lognormal CSD (circles), simulated in GALOPER by LPE growth (Eq. 3; GALOPER option 5), with lognormal fit (line). (B) CSD in (A) is doubled in size by supply controlled growth (solid circles; GALOPER option 6) and by multiplication of the crystal sizes by 2 (open circles). (C) CSD in (A) is doubled in size by adding 10 nm to each crystal size. (D) CSD in (A) is Ostwald ripened (GALOPER closed system option 1), allowing 1% of the crystal mass to pass through solution.

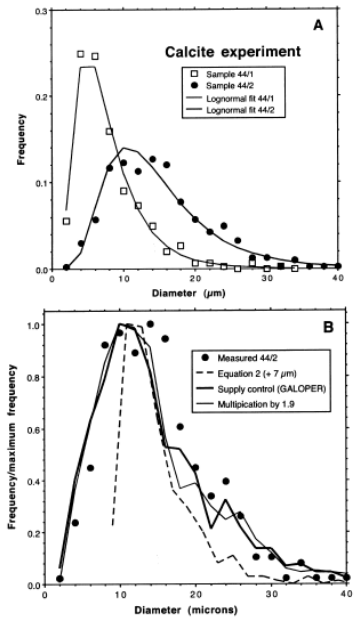

FIGURE 3. CSDs measured (Kile et al. 2000) and calculated for calcite growth experiments. (A) Initial, measured CSD (CCNG-44/1; squares) and final, measured CSD (CCNG-44/2; circles) with lognormal fits (solid lines). The two calcites were taken from the same solution after different reaction times. (B) The final, normalized, measured CSD (CCNG-44/2; circles) modeled from the initial CSD (CCNG-44/1) by Equation 2 (broken line), by supply controlled modification of Equation 3 using the GALOPER program (thick solid line), and by multiplying by a constant (thin solid line).

Ivanov, V.K., Fedorov, P.P., Baranchikov, A.Y., and Osiko, V.V. (2014) Oriented attachment of particles: 100 years of investigations of non-classical crystal growth. Russian Chemical Reviews 83, 1204-1222.

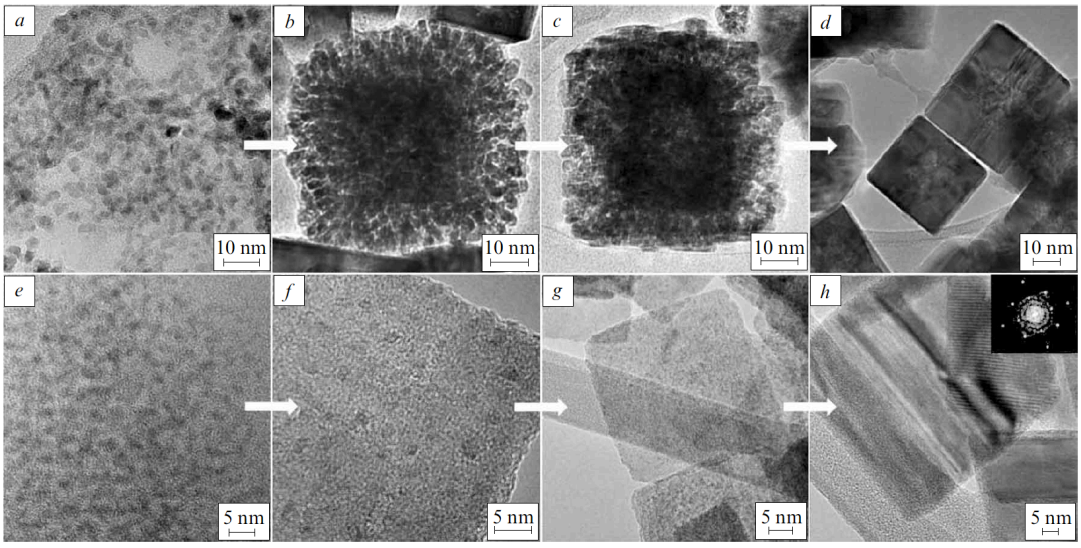

Figure 12. TEM images reflecting the sequence of stages in the oriented attachment of nanocrystals.[140]
(*a*) Original FeS_2 crystals, (*b*) agglomeration of crystallites, (*c*) attachment of crystallites, (*d*) recrystallization to form cubic single crystals, (*e*–*h*) formation of thin FeS_2 plates as a result of attachment and recrystallization processes.

Kile, D. and Eberl, D. (1999) Crystal growth mechanisms in miarolitic cavities of the Lake George ring and vicinity, Colorado. American Mineralogist, 84, 718-724.

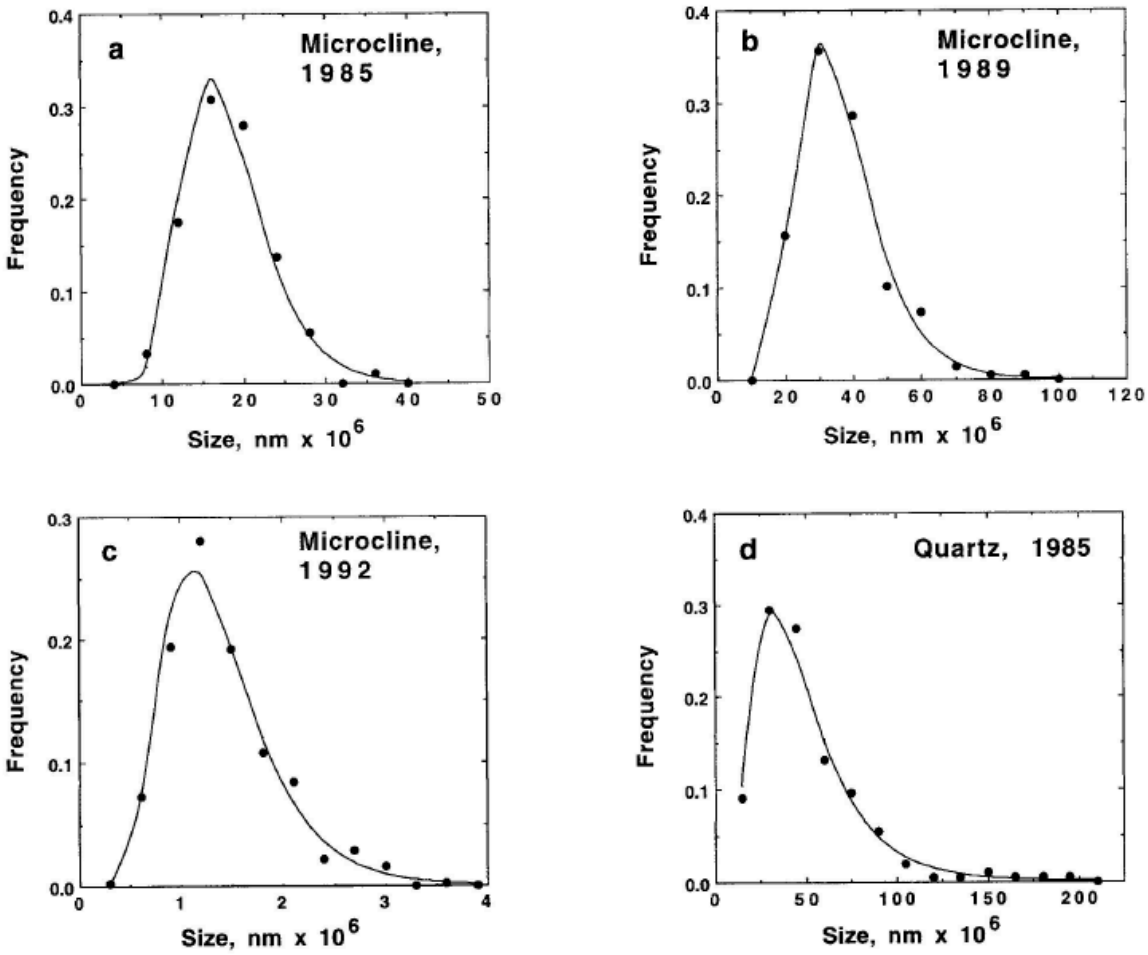

FIGURE 2. Representative plots showing CSDs superimposed on the theoretical lognormal curves (solid lines): (a) microcline, LGR, 1985; (b) microcline, LGR, 1989; (c) microcline, north of LGR, 1992; and (d) quartz, LGR, 1985.

Kile, D. and Eberl, D. (2003) On the origin of size-dependent and size-independent crystal growth: Influence of advection and diffusion. American Mineralogist, 88, 1514-1521.

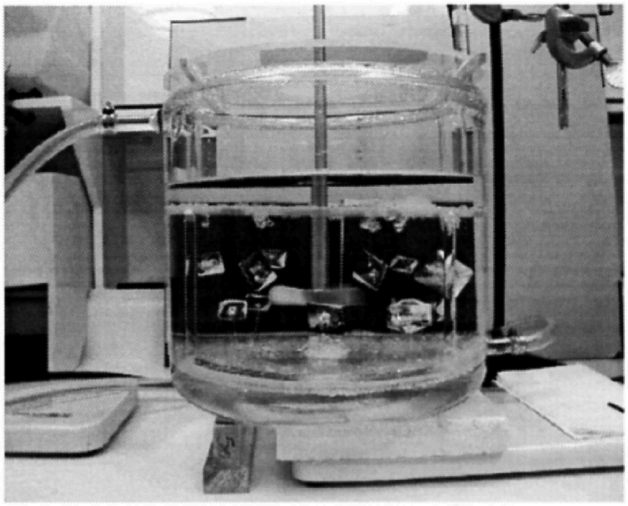

FIGURE 1. Water-jacketed crystallization vessel with variable-speed stirrer for alum experiments.

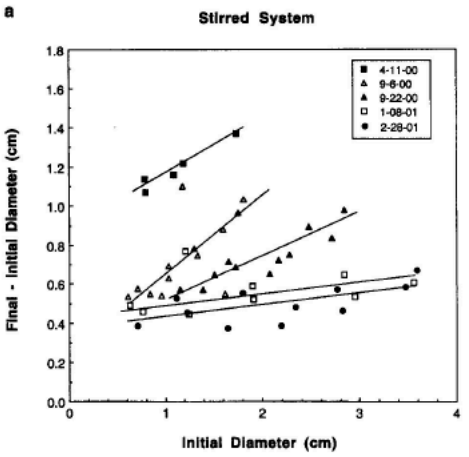

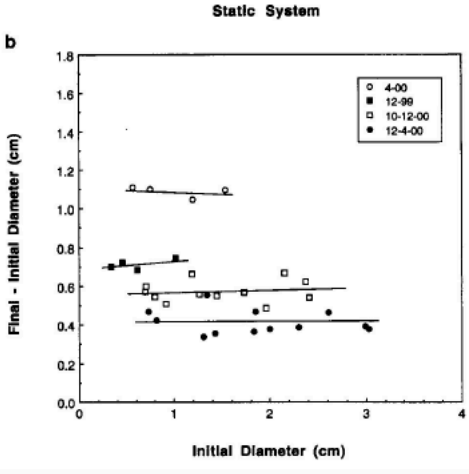

FIGURE 2. Growth rate as a function of initial crystal size measured for (a) stirred and (b) unstirred systems for alum crystals.

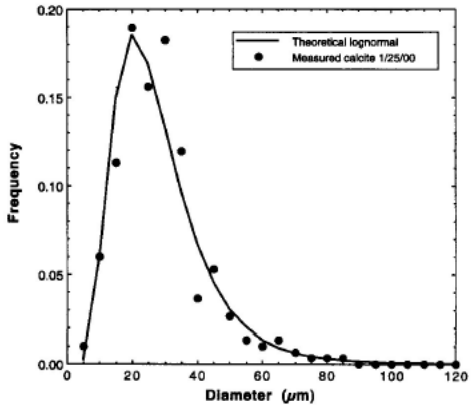

FIGURE 3. CSD for calcite formed in a non-stirred system, with theoretical lognormal curve.

Figure 4C

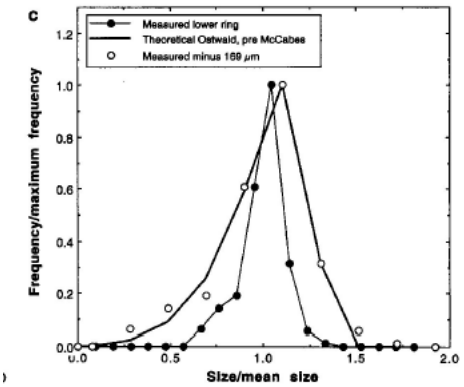

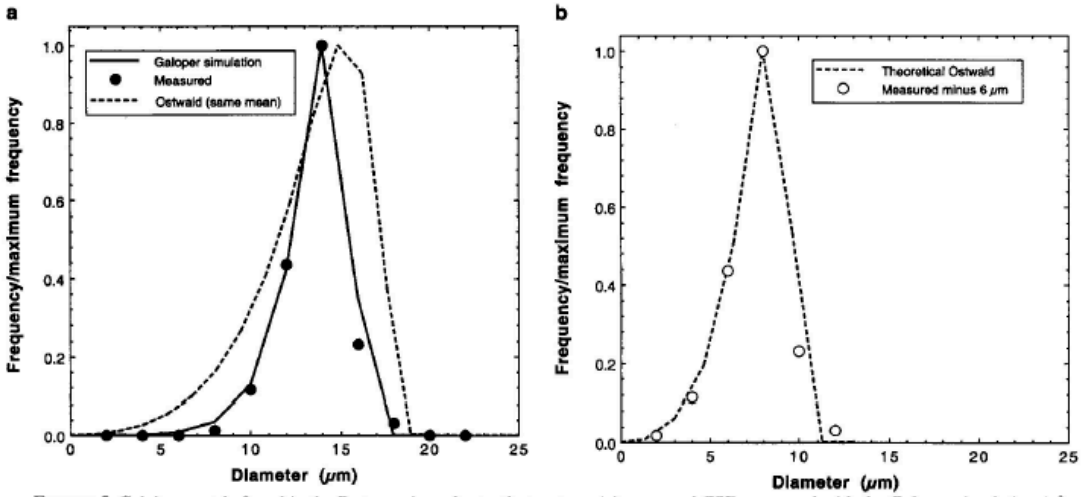

FIGURE 5. Calcite crystals found in the Proterozoic molar tooth structure: (a) measured CSD compared with the Galoper simulation ($\chi^2 > 20\%$) and the theoretical CSD expected for Ostwald ripening; (b) measured CSD with constant growth stage subtracted from the crystal sizes compared with the theoretical Ostwald curve.

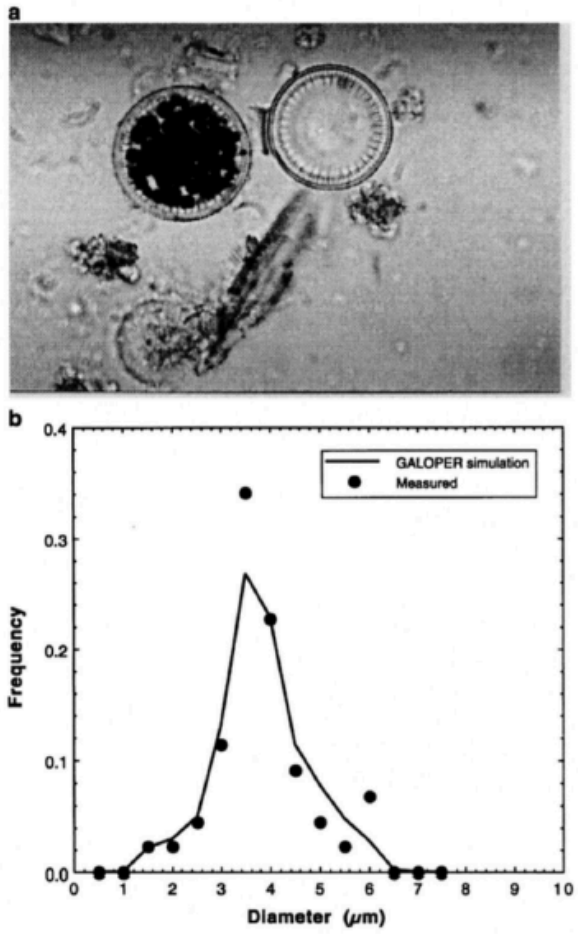

FIGURE 6. Greigite (?) from Pyramid Lake, Nevada: (a) photomicrograph of crystals found within diatom tests, and (b) CSD measured for crystals compared with a Galoper simulation (χ^2 significance >20%).

Kile, D., Eberl, D., Hoch, A., and Reddy, M. (2000) An assessment of calcite crystal growth mechanisms base on crystal size distributions. Geochimica et Cosmochimica Acta, 64, 2937-2950.

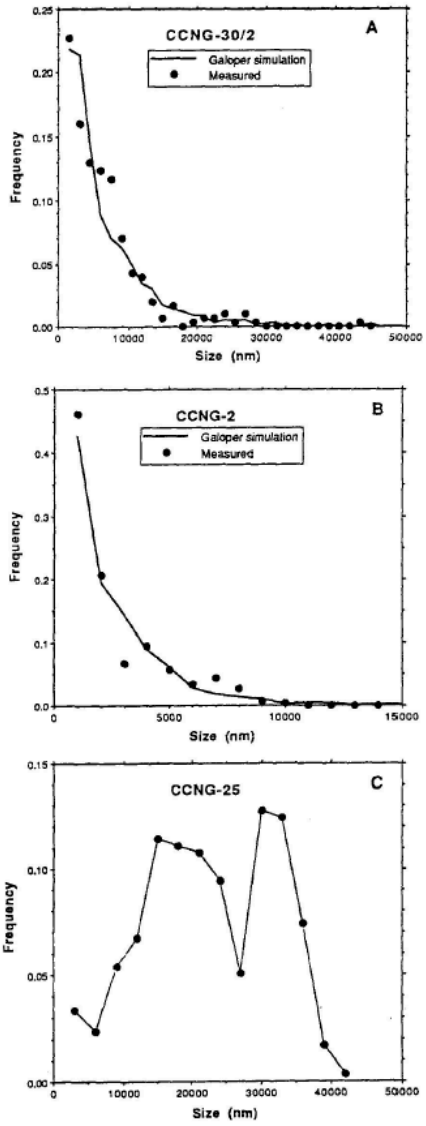

Fig. 2. (A) Characteristic asymptotic CSD for sample CCNG-30/2. The Galoper simulation used a critical nucleus size of 3 nm (read from Fig. 10, using $\Omega = 20$ from Table 1) with 143 crystals nucleating per calculation cycle, followed by supply-controlled growth to the correct mean size; level of significance for χ^2 comparison between simulated and measured CSDs = 2.5 to 5%. (B) Characteristic asymptotic CSD for sample CCNG-2. CSD simulated as in A, with significance level = 1 to 5%. (C) Bimodal CSD resulting from sequential addition of $CaCl_2$ and KOH for sample CCNG-25.

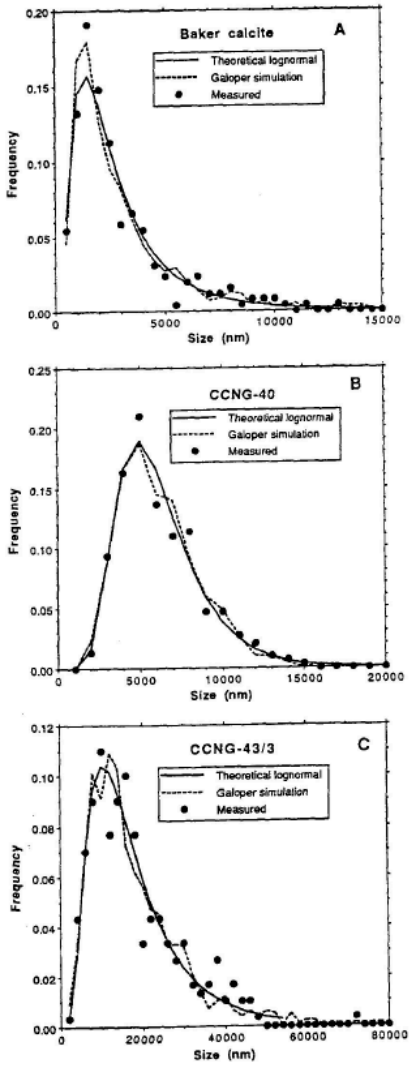

Fig. 3. (A) Plot of size vs. frequency showing lognormal CSD for Baker calcite. Galoper simulation used a critical nucleus size of 3 nm and a probability for nucleation of 0.6, followed by supply-controlled growth; significance level for χ^2 comparison between simulation and measurements = 10 to 20%. (B) Plot of size vs. frequency for a typical lognormal profile of synthetically grown calcite (CCNG-40). Galoper simulation used a critical nucleus size of 2.5 nm (Table 1 and Fig. 10) and a probability for nucleation of 0.85, followed by supply-controlled growth; significance level > 20%. (C) Plot of size vs. frequency for a typical lognormal profile of synthetically grown calcite (CCNG-43/3). Galoper simulation used a critical nucleus size of 3 nm (Table 1 and Fig. 10), and a probability for nucleation of 0.60; significance level > 20%.

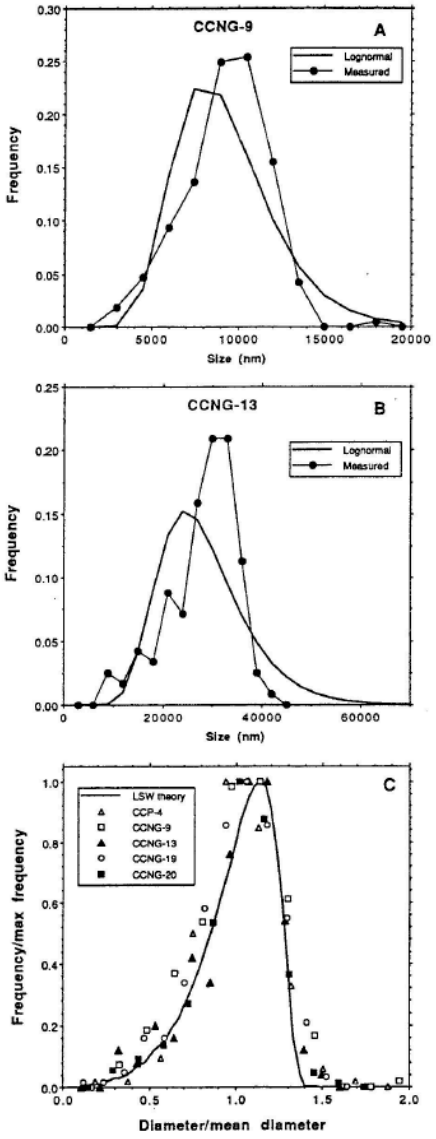

Fig. 4. (A) Negatively skewed CSD characteristic of Ostwald ripening (CCNG-9). (B) Negatively skewed CSD characteristic of Ostwald ripening (CCNG-13). (C) Reduced plot showing ripened samples with the theoretical, universal, steady-state curve expected for diffusion-controlled Ostwald ripening according to the LSW theory, with ripened samples.

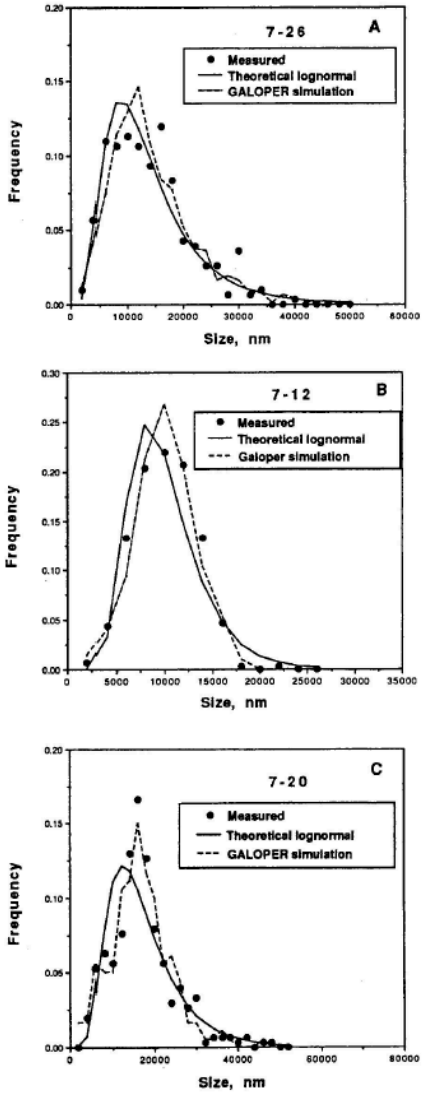

Fig. 5. (A) Transitional CSD (sample 7-26) with a shape that is intermediate between lognormal and Ostwald curves. Starting Ω = 28.2. χ^2 significance between experimental data and Galoper simulation = 5 to 10%. (B) Transitional CSD (sample 7-12) with a shape that is intermediate between lognormal and Ostwald curves. Starting Ω = 53.7. χ^2 significance between experimental data and Galoper simulation = 10 to 20%. (C). Transitional CSD (sample 7-20) with a shape that is intermediate between lognormal and Ostwald curves. Starting Ω = 69.2. χ^2 significance between experimental data and Galoper simulation = > 20%.

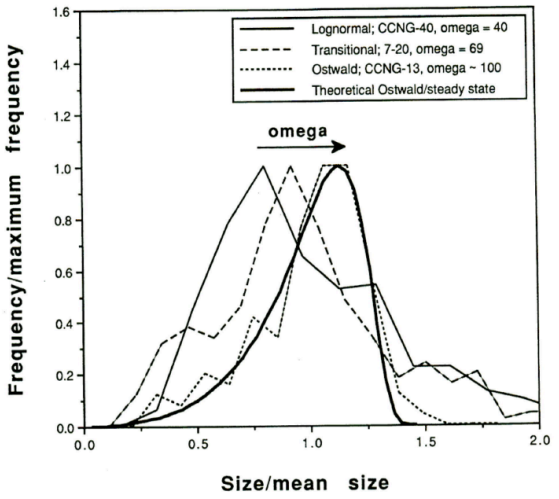

Fig. 6. Reduced plot of lognormal, transitional, and Ostwald CSDs showing a progressive shift with increasing Ω toward the theoretical Ostwald steady-state curve.

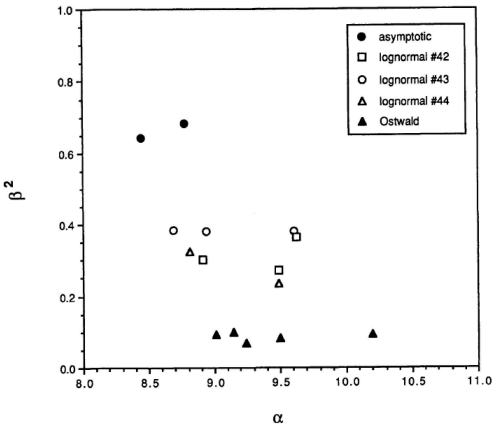

Fig. 7. Plot of size variance (β^2) vs. natural log mean size (α) for synthetic calcite.

A.

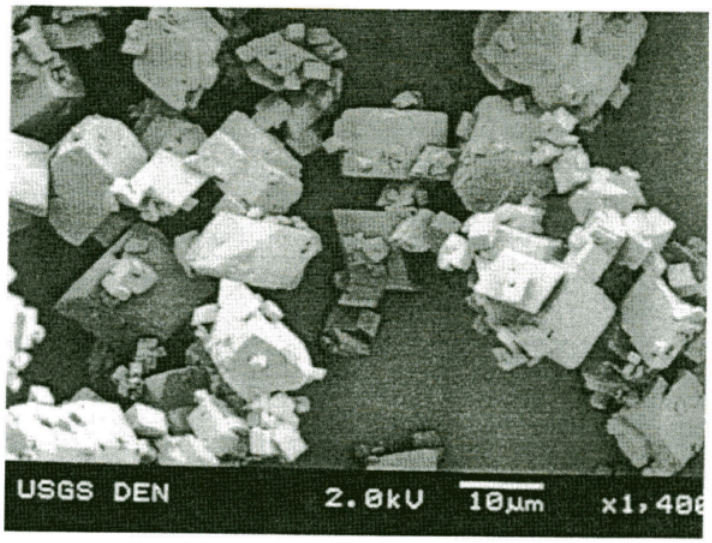

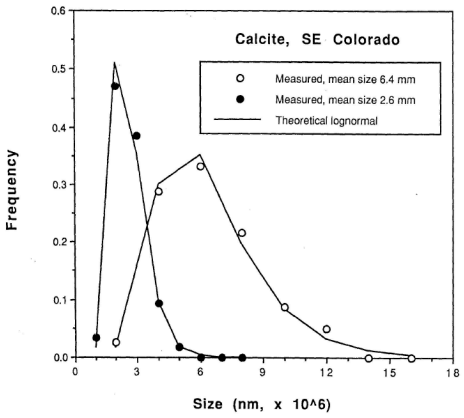

Fig. 9. Lognormal size distributions for two naturally occurring calcite samples from southeastern Colorado.

B.

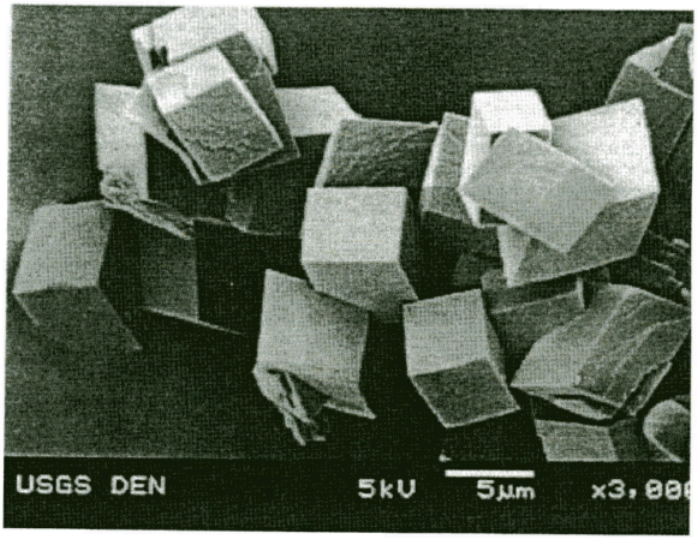

Fig. 8. (A) SEM photo of synthetic calcite (Baker) illustrating a lognormal CSD with large size variance ($\beta^2 = 0.52$). (B) SEM photo of synthetic calcite (CCNG-19) illustrating an Ostwald CSD with a small size variance ($\beta^2 = 0.09$).

Table 1. Summary of experimental methods and conditions for calcite crystal growth experiments.

Sample no.	CSD shapes	Initial vol. (mL)	Initial concentration (M) $CaCl_2$	$NaHCO_3$	Na_2CO_3	KNO_3	NaCl	Excess (mL) $CaCl_2$ + KOH	Start pH[a]	Final pH	Duration	Calculated initial Ω	Final Ω
CCNG-2	asymptotic	150	0.0020	0.002		0.093		15	8.5	8.5	100 min	20	22.3
CCNG-30	asymptotic	300	0.0020	0.002		0.093		30	8.5	8.4	195 min	20	17.2
CCNG-35	lognormal	300	0.0020	0.002		0.093		30	8.8	8.7	140 min	30	24
CCNG-40	lognormal	300	0.0020	0.002		0.093		67	8.7	8.4	30 min[a]	40	19
CCNG-42	lognormal	300	0.0020	0.002		0.093		45	8.7	8.5	7 hours[a]	32	21
CCNG-43	lognormal	300	0.0020	0.002		0.093		33	8.6	8.5	230 min[a]	22	18
CCNG-44	lognormal	300	0.0020	0.002		0.093		32	8.6	8.5	5 hours	22	17
CCNG-45	lognormal	300	0.0020	0.002		0.093		64	8.8	8.5	225 min[a]	41	26
CCNG-9	Ostwald	100	0.0265	0.002	0.0244	0.046			10.7	10.0	~1 min	3090[c]	[b]
CCNG-13	Ostwald	100	0.0265	0.002	0.0244	0.046			10.7	8.4	14 hours	3090[c]	42
CCNG-19	Ostwald	400	0.0050		0.0050		0.50		10.5	10.0	40 min	106	67
CCNG-20	Ostwald	200	0.0265	0.002	0.0244	0.046			10.5	8.1	90.5 hours	3090[c]	2
CCP-4[d]	Ostwald	400	0.0020	0.002		0.093			8.5	8.5	45 hours	5	5
7-26	transitional	400	0.0025		0.0025	0.025	0.25		10.3	10.3	53 min	28.2	[b]
7-12	transitional	400	0.0038		0.0050	0.05	0.50		10.5	10.5	50 min	53.7	[b]
7-20	transitional	400	0.0050		0.0050	0.05	0.50		10.3	10.3	49 min	69.2	[b]
CCNG-25	bimodal		0.0050	0.005			0.50		9.9	9.7	105 min	51.4	10.5

[a] In lognormal experiments, the time listed is the time from highest pH to final sampling.
[b] Ca^{2+} concentration data not available for calculation.
[c] Actual value of omega does not exceed ~100 due to short induction time.
[d] Constant composition experiment using CCNG-19 crystals as seed.

Table 2. Crystal size distribution data and statistical evaluation for calcite crystal growth experiments; horizontal lines indicate continuous growth experiments.

CSD shape	Sample no.	α	β^2	Group size	Average size (nm)	Lognormal significance, χ^2 test
asymptotic	CCNG-30/2	8.45	0.64	1,500	6,420	NA
asymptotic	CCNG-30/3	8.78	0.68	1,700	8,864	NA
asymptotic	CCNG-2	7.60	0.52	1,000	2,585	NA
lognormal	CCNG-42/1	8.91	0.30	1,000	8,500	2.5–5
~lognormal	CCNG-42/2	9.49	0.27	2,000	14,870	<1
lognormal	CCNG-42/3	9.62	0.36	1,500	17,810	10–20
lognormal	CCNG-43/1	8.69	0.38	2,000	7,140	>20
lognormal	CCNG-43/2	9.00	0.49	2,000	10,320	1–5
lognormal	CCNG-43/3	9.61	0.38	2,000	17,853	>20
lognormal	CCNG-44/1	8.81	0.32	2,000	7,950	>20
lognormal	CCNG-44/2	9.49	0.23	2,000	14,800	>20
lognormal	CCNG-40	8.65	0.16	1,000	6,200	>20
lognormal	CCNG-45/3	9.33	0.25	2,700	12,690	10–20
lognormal	CCNG-35	9.03	0.32	2,000	9,770	>20
lognormal	Baker calcite	7.72	0.59	500	2,944	10–20
Ostwald	CCNG-9	9.14	0.10	1,500	9,359	NA
Ostwald	CCNG-13	10.20	0.09	3,000	28,080	NA
Ostwald	CCNG-19	9.01	0.09	1,000	8,522	NA
Ostwald	CCNG-20	9.50	0.08	2,000	13,792	NA
Ostwald	CCP-4	9.24	0.07	2,000	10,640	NA
transitional	7-26	9.40	0.31	2,000	13,953	NA
transitional	7-12	9.15	0.13	2,000	10,040	NA
transitional	7-20	9.65	0.24	2,000	17,294	NA
bimodal	CCNG-25	9.93	0.25	3,000	22,812	NA

NA = not applicable.